TXNDC5 Governs Extracellular Matrix Homeostasis in Pulmonary Hypertension

Zhen Chen[1*]; Fanhao Kong[1*]; Lixin Huang[1*]; Wenze Wu[1*]; Ziping Wang[1]; Hanbin Chen[1]; Junting Zhang[1]; Lin Deng[6]; Chengrui Cao[1]; Xiaoyan Zhang[1]; Zixin Liu[2]; Kai-Chien Yang[3#]; Wei-Ting Chang[4, 5#]; Jin-Song Bian[1#]; Xiaowei Nie[2#];

1 Department of Pharmacology, Joint Laboratory of Guangdong-Hong Kong Universities for Vascular Homeostasis and Diseases, SUSTech Homeostatic Medicine Institute, School of Medicine, Southern University of Science and Technology, Shenzhen 518055, China.

2 Department of Human Cell Biology and Genetics, SUSTech Homeostatic Medicine Institute, School of Medicine, Southern University of Science and Technology, Shenzhen 518055, China.

3 Department and Graduate Institute of Pharmacology, National Taiwan University College of Medicine, Taipei, Taiwan

4 School of Medicine, College of Medicine, National Sun Yat-sen University, Kaohsiung, Taiwan

5 Division of Cardiology, Department of Internal Medicine, Chi Mei Medical Center, Tainan

6 Department of Cardiology, The Eighth Affiliated Hospital, Sun Yat-sen University, Shenzhen, China

[*]These authors contributed equally to this work.

[#]Correspondence to:

Xiaowei Nie, PhD, E-mail niexw@sustech.edu.cn.

Jin-Song Bian, PhD, E-mail bianjs@sustech.edu.cn.

Wei-Ting Chang, PhD, E-mail cmcvecho2@gmail.com.

Kai-Chien Yang, PhD, E-mail allenmy0920@gmail.com.

ABSTRACT

BACKGROUND: Pulmonary hypertension (PH) is characterized by vascular remodeling without effective treatments. Thioredoxin domain containing 5 (TXNDC5), a member of the protein disulfide isomerases (PDI) family, regulates protein folding and vascular homeostasis, yet its role in PH remains unknown.

METHODS: Label-free proteomics profiled protein expression in lungs from PH patients. TXNDC5 was analyzed by single-cell RNA sequencing, immunofluorescence, and Western blot. Endothelial gain- and loss-of-function approaches were applied in Sugen5416/hypoxia (SuHx)-induced rodent PH models. RNA sequencing and protein-protein interaction analysis were used to investigate underlying mechanisms.

RESULTS: TXNDC5 was significantly upregulated in the lungs of patients with PH and in experimental PH models, with predominant localization in endothelial cells (ECs) of remodeled distal pulmonary arteries. Endothelial TXNDC5 overexpression exacerbated pulmonary vascular remodeling, elevated right ventricular systolic pressure, and promoted right ventricular hypertrophy, whereas global or endothelial-specific TXNDC5 deficiency conferred protection against SuHx-induced PH. Hypoxia-induced factor (HIF)-2α transcriptionally activated TXNDC5 to drive PH development. Single-cell RNA sequencing identified a distinct subpopulation characterized by TXNDC5^{high} extracellular matrix (ECM)-producing ECs. Bulk RNA sequencing combined with protein-protein interaction analysis revealed that TXNDC5 regulated ECM homeostasis through biglycan (BGN). Pharmacological inhibition of TXNDC5 with E64FC26 and endothelial-targeted TXNDC5 gene therapy significantly attenuated PH severity in rats.

CONCLUSIONS: Our study reveals that TXNDC5 is a main modulator to regulate ECM homeostasis and may serve as a promising target for the treatment of PH.

Key Words: pulmonary hypertension**,** extracellular matrix, TXNDC5, BGN, HIF signaling

60 **INTRODUCTION**

61 Pulmonary hypertension (PH) is a serious cardiovascular disease characterized by
62 elevated pulmonary artery pressure and right heart failure, with high morbidity and
63 mortality[1]. Dysfunction of pulmonary artery endothelial cells (PAECs) under hypoxia
64 initiates vasoconstriction[2], while pulmonary artery smooth muscle cells (PASMCs)
65 become hyperproliferative and apoptosis-resistant phenotype, leading to vascular
66 remodeling[3]. However, there remains no curative clinical treatment option for reversing
67 remodeled vessels against the disease[4,5]. It highlights the need for further exploration
68 of PH pathogenesis and new therapeutic targets.

69 Protein disulfide isomerase (PDI) is an endoplasmic reticulum enzyme family that
70 mediates disulfide bond formation, protein folding, and regulates endothelial function
71 to maintain vascular homeostasis[6,7]. Thioredoxin domain containing 5 (TXNDC5),
72 mainly expressed in endothelial cells (ECs) and also called endothelial PDI, is linked
73 to fibrosis[8], diabetes[9], rheumatoid arthritis[10], and cancers[11]. Inhibition of TXNDC5
74 restores endothelial dysfunction to mitigate vascular calcification and
75 atherosclerosis[12,13]. However, its role in pulmonary vascular remodeling in PH remains
76 unclear.

77 Extracellular matrix (ECM) is a complex network of proteins and polysaccharides
78 secreted by cells, providing structural and communicative support to adjacent cells[14].
79 Remodeling of pulmonary arterial ECM occurs in the early stage of PH pathogenesis,
80 before increased wall thickness and pulmonary artery pressure. ECM remodeling is the
81 cause rather than a consequence of pulmonary vascular remodeling in PH[15]. Recently,
82 we revealed that the ECM proteins in PAECs accelerated pulmonary vascular
83 remodeling through interaction with hypoxia-induced factor (HIF)-1α in a positive
84 feedback loop manner, providing evidence for early intervention in ECM remodeling
85 to prevent PH progression[16,17].

86 In this study, we identified TXNDC5 as a markedly dysregulated factor in ECs
87 within the pulmonary vasculature in PH. Global or endothelial-specific deficiency of
88 TXNDC5 alleviated Sugen5416/hypoxia (SuHx)-induced PH, whereas TXNDC5

overexpression aggravated PH. HIF-2α was identified as a transcriptional activator of TXNDC5. Single-cell RNA sequencing identified a distinct subpopulation characterized by TXNDC5^{high} ECM-producing ECs. TXNDC5 directly interacts with biglycan (BGN) and facilitates its folding, thereby promoting pathological ECM remodeling. Pharmacological inhibition or pulmonary endothelium-targeted silencing of TXNDC5 effectively mitigated PH in rats. The present study demonstrated that TXNDC5 may be a key protein to control ECM homeostasis and a promising therapeutic target for PH.

METHODS

Expanded methods and materials are available in **Supplemental Material 1**.

Data Availability Statement

Source data and original blots or gel images for this study are available from the corresponding author upon reasonable request.

RESULTS

TXNDC5 Expression is Increased in PH Patients and Rodent Models

We performed 4D label-free proteomic profiling of lung tissues from 5 patients with PH and 5 non-PH donors (**Figure 1A** and **Supplemental Material 2**). Among the human PDI family proteins, TXNDC5 was the most markedly dysregulated protein in PH patients compared with donor controls (fold change=3.45, P=0.0048) (**Figure 1B**). Consistently, increased TXNDC5 protein levels in lungs from PH patients were confirmed (**Figure 1C**), and similar results were recapitulated in multiple rat and mouse PH models (**Figure 1D** and **Figure S1A-B**).

To examine the cellular localization of TXNDC5 in PH, we analyzed a single-cell RNA sequencing dataset (GSE273062) from lung tissues of SuHx-exposed rats and normoxic controls (Nor) (**Figure 1E-F**). TXNDC5 was primarily expressed in ECs

(**Figure 1G**) and was markedly upregulated in ECs from SuHx lungs compared with controls (**Figure 1H**). Western blot analysis of primary lung ECs corroborated these findings (**Figure 1I-J**). In pulmonary arteries from human lungs, multiplex immunofluorescence revealed strong co-localization of TXNDC5 with the endothelial marker CD31. Moreover, TXNDC5 expression was markedly increased in the intimal layer of remodeled pulmonary arteries from PH patients (**Figure 1K**). Taken together, these findings suggest that the TXNDC5 may be a critical dysregulated factor in ECs within the pulmonary vasculature that contributes to PH pathogenesis.

TXNDC5 Mediates the Development of SuHx-Induced PH

To investigate the role of TXNDC5 *in vivo* in the development of experimental PH, TXNDC5 knockout (TXNDC5$^{-/-}$) mice were challenged with or without SuHx (**Figure 2A**). TXNDC5 deletion alone had no significant effects but markedly reduced RVSP (**Figure 2B**) and Fulton index (right ventricle weight to left ventricle plus interventricular septum weight, ie, RV/(LV+S)) (**Figure S1C**) induced by SuHx. Echocardiography indicated improved right ventricular (RV) function, with increased pulmonary artery acceleration time/ pulmonary artery ejection time ratio (PAT/PET), tricuspid annular plane systolic excursion (TAPSE), and right ventricular fractional area change (RVFAC), along with reduced right ventricular free wall thickness (RVFWT) (**Figure S1D**). In addition, H&E and α-SMA staining demonstrated attenuation of distal pulmonary artery medial wall thickening and muscularization under SuHx (**Figure 2C-D**). Consistent with the pulmonary arterial changes, wheat germ agglutinin (WGA) staining proved that the RV cardiomyocyte hypertrophy was markedly inhibited in SuHx-treated TXNDC5$^{-/-}$ mice when compared with their control littermates (**Figure 2E**).

With a gain-of-function approach, an adeno-associated virus (AAV) serotype engineered to specifically target lung ECs was delivered via the tail vein to overexpress TXNDC5 specifically (AAV-TXN) (**Figure 2F**). *Ex vivo* imaging confirmed lung targeting (**Figure 2G**), and Western blot verified endothelial-specific overexpression (**Figure 2H**). In response to the SuHx challenge, AAV-TXN mice further increased in

both RVSP and RV/(LV+S) (**Figure 2I** and **Figure S1E**). Echocardiography analysis showed reduced PAT/PET, TAPSE RVFAC, and increased RVFWT under SuHx (**Figure S1F**). Consistently, immunofluorescence staining demonstrated an increased α-SMA-positive area in distal pulmonary arteries in SuHx-treated AAV-TXN mice (**Figure 2J**). Conversely, endothelial TXNDC5 overexpression was found to exacerbate SuHx-induced PH.

Endothelial Cell-Specific Deletion of TXNDC5 Ameliorates SuHx-Induced PH

To examine the role of endothelial TXNDC5 in PH, endothelial-specific TXNDC5 knockout mice ($TXNDC5^{ECKO}$) were generated, validated (**Figure S1G**), and challenged by SuHx (**Figure 3A**). Under SuHx, $TXNDC5^{ECKO}$ mice exhibited reduced distal pulmonary arterial wall thickness and α-SMA positive area (**Figure 3B**). Deletion of endothelial TXNDC5 significantly attenuated SuHx-induced increases in RVSP (**Figure 3C**), RV/(LV+S) (**Figure 3D**), and improved RV function **(Figure S1H**). Lung angiography confirmed better intrapulmonary contrast filling in $TXNDC5^{ECKO}$ mice compared with $TXNDC5^{f/f}$ controls, indicating preserved pulmonary vasculature (**Figure 3E**). In addition, SuHx-induced RV hypertrophy was also markedly attenuated, with decreased RV wall thickness and cardiomyocyte cross-sectional area (**Figure 3F-G**). Together, these findings underscore the crucial role of endothelial TXNDC5 in the development of PH and highlight its potential as a sex-independent therapeutic target.

E64FC26 Exhibits Therapeutic Effects Against PH in Rats

E64FC26 is a potent PDI pan-inhibitor with an IC_{50} of 16.3 μM against TXNDC5[18]. To assess its safety, histological analyses were performed on major organs from rats treated with E64FC26 for 5 weeks under normoxic conditions. No pathological abnormalities were observed in the kidneys, liver, or spleen, with preserved tissue architecture and no evidence of necrosis or inflammatory infiltration (**Figure S2A**). These findings indicate that E64FC26 exhibits a favorable safety profile without causing overt organ or systemic toxicity.

To examine the therapeutic effect of TXNDC5 inhibition in PH, E64FC26 was

177 administered intraperitoneally in SuHx-induced PH rats (**Figure 4A**). E64FC26
178 administration significantly attenuated the increases of RVSP (**Figure 4B**) and
179 RV/(LV+S) ratio (**Figure 4C**) compared with vehicle-treated rats. E64FC26 reversed
180 SuHx-induced pulmonary arterial muscularization (**Figure 4D**) and wall thickness
181 (**Figure 4E**). In addition, histological analyses revealed that E64FC26 markedly
182 alleviated RV hypertrophy in SuHx-induced PH rats (**Figure 4F**). Echocardiographic
183 assessment further demonstrated improved RV function following E64FC26 treatment
184 (**Figure S2B**).

185 To determine whether the therapeutic effects of E64FC26 in PH are mediated
186 primarily through TXNDC5 rather than off-target inhibition of other PDI family
187 members, $TXNDC5^{ECKO}$ mice were treated with E64FC26 under SuHx conditions
188 (**Figure S2C**). E64FC26 did not provide additional protection in TXNDC5 endothelial-
189 deficient mice, as distal pulmonary arterial remodeling remained unchanged compared
190 with vehicle-treated $TXNDC5^{ECKO}$ mice (**Figure 4G**). Lung angiography further
191 showed no improvement in distal pulmonary perfusion following E64FC26 treatment
192 (**Figure 4H**). Consistently, E64FC26 failed to attenuate RVSP elevation (**Figure S2D**),
193 RV hypertrophy (**Figure S2E**), and RV dysfunction (**Figure S2F**) in SuHx-treated
194 $TXNDC5^{ECKO}$ mice. These findings indicate that the therapeutic efficacy of E64FC26
195 in PH is largely dependent on endothelial TXNDC5, supporting pharmacological
196 inhibition of TXNDC5 as a promising strategy for PH treatment.

197

198 **Pulmonary Endothelium-Targeted TXNDC5 Gene Therapy Ameliorates PH**

199 We further established a pulmonary endothelium-targeted gene therapy approach
200 to enhance organ specificity. Using a self-complementary adeno-associated virus
201 (scAAV) vector encoding shRNA against TXNDC5 (shTXN), we achieve rapid and
202 endothelial-specific gene silencing *in vivo*. The vector was administered via the tail vein
203 to SuHx-induced PH rats to selectively suppress TXNDC5 in lung ECs (**Figure 4I**). *Ex*
204 *vivo* imaging confirmed efficient lung targeting (**Figure 4J**), and Western blotting
205 showed marked TXNDC5 suppression in primary rat lung ECs (**Figure S2G**).

206 Treatment with shTXN significantly attenuated SuHx-induced pulmonary arterial

remodeling compared with the control vector (shNC) (**Figure 4K**). Hemodynamic measurements showed reduced RVSP following shTXN administration (**Figure 4L**). Moreover, morphological and histological analyses showed that shTXN decreased the RV/(LV+S) ratio (**Figure S2H**) and alleviated RV wall thickening (**Figure 4M**). Consistently, echocardiographic assessment revealed improved RV function (**Figure S2I**). Collectively, these results demonstrate that endothelial-targeted TXNDC5 silencing effectively mitigates pulmonary vascular remodeling and right heart dysfunction in PH, highlighting the therapeutic potential of TXNDC5 inhibition.

TXNDC5 Promotes Hypoxia-Induced Dysfunction in PAECs

Exposure to hypoxia significantly increased the TXNDC5 protein and mRNA levels in PAECs (**Figure S3A-B**), predominantly in the cytoplasm (**Figure S3C**). Silencing TXNDC5 with small-interfering RNA oligonucleotides (siTXNDC5) suppressed proliferation (**Figure S3D**) and migration (**Figure S3E**) of PAECs under both normoxic and hypoxic conditions, and prevented G1-to-S phase transition (**Figure S3F**). Conversely, TXNDC5 overexpression via lentivirus (LV-TXNDC5) disrupted cytoskeletal architecture, inducing prominent stress fibers and diffuse paxillin distribution (**Figure S3G-H**). Taken together, TXNDC5 regulates important functional abnormalities associated with PH pathogenesis, with disruption of cytoskeletal architecture in PAECs.

HIF-2α Transcriptionally Activates TXNDC5 to Drive Pulmonary Hypertension

As an endothelial-specific hypoxia-responsive transcription factor, HIF-2α has been considered a critical regulator of pulmonary vascular remodeling in PH[19]. We examined the HIF-2α activity based on the single-cell RNA sequencing dataset (GSE273062) and found that it was markedly elevated in ECs from SuHx-treated rat lungs compared with those from normoxic controls (**Figure 5A**). Consistently, immunofluorescence staining of remodeled pulmonary arteries from patients with PH revealed pronounced nuclear accumulation of HIF-2α within ECs, accompanied by robust expression of TXNDC5 (**Figure 5B**). These findings implicate HIF-2α as a

transcriptional activator of TXNDC5 in pulmonary arterial ECs during PH. To further determine whether TXNDC5 is a direct transcriptional target of HIF-2α, we analyzed the promoter region of TXNDC5 and identified two putative HIF-2α binding sites (BS1 and BS2) (**Figure 5C**). Chromatin immunoprecipitation (ChIP) assays confirmed that HIF-2α bound to both sites in the TXNDC5 promoter (**Figure 5D**). Consistently, dual-luciferase reporter assays demonstrated that mutation of either binding site significantly reduced TXNDC5 promoter activity, whereas simultaneous mutation of both sites caused a further decrease (**Figure 5E**). These results indicate that BS1 and BS2 cooperatively mediate HIF-2α-driven transcriptional activation of TXNDC5.

Next, to mimic sustained HIF-2α activation independent of hypoxia, we utilized a HIF-2α (dPA) mutant in which Pro405 and Pro531 were substituted with alanine (A)[20], allowing it to escape Von Hippel-Lindau-mediated degradation and stable expression under normoxic conditions (**Figure 5F**). Immunofluorescence staining showed that lentiviral delivery of HIF-2α (dPA) resulted in prominent nuclear accumulation of HIF-2α in PAECs (**Figure 5G**). Quantitative polymerase chain reaction (qPCR) analysis further demonstrated that HIF-2α overexpression significantly increased the mRNA levels of TXNDC5, together with induction of canonical HIF target genes, including vascular endothelial growth factor A (VEGFA) and endothelin-1 (EDN1). (**Figure S4A**). Western blot analysis confirmed robust HIF-2α overexpression and a concomitant increase in TXNDC5 protein levels (**Figure 5H**). Moreover, HIF-2α silencing abolished the hypoxia-induced upregulation of TXNDC5, indicating that HIF-2α was required for hypoxia-driven TXNDC5 induction (**Figure S4B**).

Next, to assess the *in vivo* functional importance of the HIF-2α-TXNDC5 axis, we overexpressed endothelial HIF-2α (dPA) in both $TXNDC5^{f/f}$ and $TXNDC5^{ECKO}$ mice (**Figure 5I**). Notably, without hypoxia exposure, overexpression of HIF-2α (dPA) was sufficient to induce a mild PH phenotype in $TXNDC5^{f/f}$ mice, as evidenced by elevated right RVSP, increased pulmonary arterial remodeling, and RV hypertrophy. Importantly, these pathological changes were largely abolished in $TXNDC5^{ECKO}$ mice, demonstrating that endothelial TXNDC5 is required for HIF-2α-driven pulmonary vascular remodeling and PH development (**Figure 5J-L** and **Figure S4C**). These

267 findings indicate that TXNDC5 is a critical downstream mediator of HIF-2α-driven
268 pathological remodeling in the pulmonary vasculature.
269
270 **TXNDC5 Regulates ECM Expression and Homeostasis**
271 To explore the downstream molecular mechanisms of TXNDC5, we reclustered
272 ECs from the previously single-cell RNA-seq dataset, identifying three
273 transcriptionally distinct subpopulations (**Figure 6A-B**). Cluster 1 was annotated as
274 homeostatic gas-exchange homeostatic ECs, characterized by genes associated with
275 capillary specialization and endothelial quiescence, including *Ca4*, *Cldn5*, *Apln*, *Kdr*,
276 and *Selenop*. The second subset exhibited a transcriptional profile indicative of
277 cytoskeletal remodeling and ECM interaction, with prominent expression of *Myo10*,
278 *Itga1*, *Col4a1*, *Fabp4*, and *Adamts9*, and was defined as remodeling-primed transitional
279 ECs (**Figure 6C**). Cluster 3 displayed robust upregulation of ECM components,
280 including *Fn1*, *Vcan*, *Bgn*, and *Ccn2*, and functional enrichment analysis of its top 200
281 marker genes further confirmed a significant association with ECM-related terms, such
282 as extracellular region and ECM (**Figure 6D**). Notably, TXNDC5 expression was
283 selectively enriched in this subset, defining a TXNDC5^{high} ECM-producing ECs
284 population (**Figure 6E-F**). Trajectory inference analysis revealed a progressive
285 transition from the gas-exchange homeostatic ECs toward the TXNDC5^{high} ECM-
286 producing ECs phenotype (**Figure 6G**). Collectively, these data suggest that PH is
287 associated with the emergence of a distinct endothelial subpopulation characterized by
288 high TXNDC5 expression and linked to ECM remodeling.
289 Next, we performed a bulk RNA sequencing (RNA-seq) analysis on PAECs
290 transfected with siRNA targeting TXNDC5 under hypoxia exposure (**Supplemental**
291 **Material 3**). Gene ontology analysis indicated that the silencing of TXNDC5 resulted
292 in altered expression of genes mainly enriched in "collagen-containing ECM", "ECM",
293 "ECM organization", "ECM structural constituent", "response to hypoxia", and
294 "cellular response to hypoxia" (**Figure 6H**). We selected the differentially expressed
295 ECM genes and then constructed a protein-protein interaction (PPI) network (**Figure**
296 **6I** and **Supplemental Material 4**). The network revealed that TXNDC5-affected ECM

297 proteins were clustered into different functional subgroups, including "proteoglycans
298 and glycoproteins", "collagens", "matrix modulators and adhesion", "metallopeptidase
299 activity", "basement membrane", "growth factors and signaling regulators", and
300 "angiogenesis". Immunofluorescence staining demonstrated markedly increased
301 periostin (POSTN) and biglycan (BGN) deposition in pulmonary arteries of $TXNDC5^{f/f}$
302 mice compared with $TXNDC5^{ECKO}$ mice after SuHx exposure (**Figure 6J-K**). Western
303 blot analysis also confirmed that TXNDC5 silencing reversed the abnormal expression
304 of ECM proteins, including collagen type I alpha 1 chain (COL1A1), transglutaminase
305 2 (TGM2), fibronectin 1 (FN1), POSTN, and lysyl oxidase (LOX) induced by hypoxia
306 treatment in PAECs (**Figure S4D**). These data indicate that endothelial TXNDC5
307 deficiency attenuates ECM accumulation. To further investigate whether TXNDC5
308 regulates ECM secretion, we collected the supernatants from PAECs. Dot blot analysis
309 revealed that the silence of TXNDC5 markedly reduced the secretion of BGN, POSTN,
310 and LOX **(Figure 6L)**. Collectively, these data highlight the key role TXNDC5 played
311 in regulating ECM homeostasis.
312 HIF signaling critically drives ECM remodeling[19]. We found that HIF-2α activity
313 was markedly increased in $TXNDC5^{high}$ ECM-producing ECs (**Figure S4E**).
314 Overexpression of HIF-2α (dPA) in PAECs induced upregulation of representative
315 ECM genes (**Figure S4F**). This increase was further confirmed at the protein level
316 (**Figure S4G**). To further determine whether endothelial TXNDC5 is required for HIF-
317 2α-induced ECM remodeling, we performed immunofluorescence staining of
318 pulmonary arteries. Overexpression of HIF-2α resulted in pronounced deposition of
319 BGN and POSTN in the pulmonary arteries of $TXNDC5^{f/f}$ mice, whereas markedly
320 attenuated in $TXNDC5^{ECKO}$ mice (**Figure S4H-I**). These results indicate that
321 endothelial TXNDC5 is required for HIF-2α-driven ECM accumulation during
322 pulmonary vascular remodeling.
323
324 **BGN Is a Promising Biomarker and Therapeutic Target for Pulmonary**
325 **Hypertension**
326 Given the complexity of the ECM network, we aimed to identify key ECM nodes

that are directly regulated by TXNDC5 and critically influence endothelial cell function. We performed a computational analysis of the PPI network by integrating an ECM protein dataset with an endothelial cell function-related protein dataset. This approach allowed us to construct a comprehensive PPI network and further refine it into a core subnetwork using degree-based filtering (**Figure 7A** and **Supplemental Material 5**). Focusing on ECM nodes from the core PPI network and ECM genes enriched in TXNDC5^{high} ECM-producing ECs, we pinpointed BGN as a central hub (**Figure 7B**). This finding positions BGN as a key mediator, capable of orchestrating the broader ECM network to modulate endothelial cell function.

We next investigated the role of BGN in PH. BGN protein levels were increased in lung biopsies from patients with PH (**Figure S5A**). Similarly, BGN was upregulated in the lungs of SuHx-treated mice (**Figure S5B**). As a circulating protein, we also investigated whether serum BGN levels can reflect the severity of PH. Surprisingly, a markedly increased serum BGN level was found in patients with PH compared with the donor controls (**Figure 7C**). Serum BGN levels exhibited a significant correlation with systolic pulmonary artery pressure (sPAP) and mean pulmonary artery pressure (mPAP) (**Figure 7D-E**), indicating its potential as a biomarker. To evaluate the role of BGN in PH generation, we generated endothelial-specific BGN knockout mice (BGN^{ECKO}) (**Figure S5C**). Notably, SuHx-induced increases in RVSP and RV/(LV+S) were significantly attenuated in BGN^{ECKO} mice compared with BGN^{flox} controls (**Figure 7F-G**). Consistently, BGN^{ECKO} mice showed reduced pulmonary arterial medial wall thickness and muscularization (**Figure 7H-I**). Lung angiogram also revealed the better-preserved lung vasculature in BGN^{ECKO} mice (**Figure 7J**). Histological assessment of the RV showed a significant reduction in hypertrophy in BGN^{ECKO} mice treated with SuHx (**Figure 7K**). Echocardiography further demonstrated that SuHx-induced decreases in PAT/PET, TAPSE, RVFAC, and increases in RVFWT were less pronounced in BGN^{ECKO} mice than in BGN^{flox} mice (**Figure S5D**). Together, our data suggest that endothelial BGN plays an important role in PH development.

TXNDC5 Assists BGN Protein Folding to Drive Pulmonary Hypertension

To elucidate how TXNDC5 regulates BGN, we first performed Western blot analysis to validate the regulatory relationship. BGN expression was markedly reduced in primary lung ECs from TXNDC5^{ECKO} mice (**Figure S5E**), whereas it was elevated in lung ECs from AAV-TXN-treated mice (**Figure S5F**), confirming that TXNDC5 positively regulates BGN. To assess the interaction between TXNDC5 and BGN, we first examined their co-localization in single-cell data, which revealed enrichment of BGN in TXNDC5^{high} ECM-producing ECs (**Figure S5G**). Subsequent immunostaining confirmed strong co-localization of TXNDC5 and BGN in PAECs (**Figure 8A**). Co-immunoprecipitation (co-IP) analysis also showed that TXNDC5 bound to BGN, and the binding was enhanced upon hypoxia exposure (**Figure 8B**). To identify the protein domain of TXNDC5 that was involved in the interaction with BGN, we performed molecular docking analysis and revealed that multiple sites of TXNDC5 (Cys89, Ser125, Gly351, and His352) might be involved in the interaction with BGN (**Figure 8C**). Thus, we constructed four TXNDC5 mutants (C89A, S125A, G351A, and H352A) and demonstrated that C89A and G351A partially abolished TXNDC5 binding with BGN (**Figure 8D**), suggesting that these amino acid residues might be essential for the binding of TXNDC5 and BGN.

As an endoplasmic reticulum resident protein with three thioredoxin domains containing CGHC motifs, TXNDC5 catalyzes disulfide bond formation[11]. Thus, we hypothesized that TXNDC5 facilitates the folding of BGN, enabling its maturation, signaling, and secretion. To test this, we generated a PDI-inactive TXNDC5 mutant (TXNDC5 Mut) with cysteine-to-alanine substitutions in all three domains. Fluorescence resonance energy transfer (FRET)-based protein folding assays showed that wild-type TXNDC5 (TXNDC5 WT) increased BGN folding efficiency, whereas TXNDC5 Mut did not (**Figure 8E-F**). Moreover, cycloheximide (CHX) chase assays further demonstrated that overexpression of TXNDC5 markedly prolonged the half-life of BGN, whereas TXNDC5 silencing accelerated BGN degradation (**Figure 8G**). These results indicate that TXNDC5 relies on its PDI activity to promote BGN folding and stability.

To assess whether BGN mediates the endothelial TXNDC5 *in vivo*, we

387 overexpressed TXNDC5 in the lung ECs of BGN^{ECKO} and BGN^{flox} mice (**Figure 8H**).
388 AAV-TXN treatment exacerbated pulmonary arterial remodeling in BGN^{flox} mice under
389 SuHx conditions, whereas this effect was largely abolished in BGN^{ECKO} mice (**Figure**
390 **8I** and **Figure S5H**). Consistently, AAV-TXN markedly increased RVSP (**Figure S5I**)
391 and aggravated RV hypertrophy in BGN^{flox} mice, whereas both changes were
392 significantly attenuated in BGN^{ECKO} mice (**Figure S5J**). Echocardiographic assessment
393 revealed that AAV-TXN led to pronounced deterioration of RV performance, while
394 these adverse functional changes were largely blunted in BGN^{ECKO} mice (**Figure S5K**).
395 Together, these results indicate that endothelial BGN is required for TXNDC5-mediated
396 PH development, confirming BGN as a key downstream effector of TXNDC5.
397

398 # DISCUSSION

399 PDI family catalyzes disulfide bond formation and rearrangement in the
400 endoplasmic reticulum. Using 4D label-free proteomics, we identified TXNDC5 as a
401 potential contributor to PH. TXNDC5, dominantly expressed in ECs, was also known
402 as endothelial PDI (Endo-PDI)[21]. We found that the silencing of TXNDC5 inhibited the
403 proliferation and migration of PAECs, whereas its overexpression led to changes in the
404 cytoskeletal architecture of PAECs, implying a critical role of TXNDC5 in endothelial
405 dysfunction in PH. *In vivo*, global or endothelial-specific TXNDC5 deletion attenuated,
406 while endothelial TXNDC5 overexpression exacerbated SuHx-induced PH.
407 Pharmacological inhibition of TXNDC5 with E64FC26 alleviated pulmonary arterial
408 remodeling and right ventricular hypertrophy, thereby preventing PH progression in
409 rats. These findings identify TXNDC5 as a promising therapeutic target for PH.

410 We next examined the molecular mechanisms of the critical role of TXNDC5 in
411 PH development. Accumulating evidence indicates that ECM remodeling, which
412 precedes pulmonary vascular remodeling, is a key driver of PH progression by altering
413 vascular stiffness and resistance[22]. In this study, through single-cell transcriptomic
414 analysis, we identified a distinct endothelial subpopulation characterized by high
415 TXNDC5 expression and a transcriptional signature enriched for ECM production and

remodeling (TXNDC5^{high} ECM-producing ECs). Subsequent bulk RNA sequencing and PPI analysis revealed that TXNDC5 broadly modulated ECM components, including proteoglycans and glycoproteins that govern matrix stiffness and elasticity, collagens that provide structural support, matrix modulators and adhesion proteins involved in ECM crosslinking, and metallopeptidases responsible for ECM turnover. TXNDC5 also influenced basement membrane proteins and angiogenesis-related factors, thereby affecting endothelial barrier function and vascular homeostasis. Notably, excessive deposition of BGN and POSTN was observed in the pulmonary arteries of SuHx-treated TXNDC5$^{f/f}$ mice but was markedly reduced in TXNDC5^{ECKO} mice. As key ECM regulators, POSTN and BGN promote matrix organization and mechanotransduction[23–25], collectively driving vascular stiffening and remodeling. These findings imply that TXNDC5 inhibition shifts the ECM equilibrium toward a less fibrotic and more compliant phenotype, mitigating PH progression by preserving vascular ECM homeostasis.

BGN has been implicated in inflammation, metabolic, musculoskeletal, and oncogenic diseases[26]. In the present study, we identified BGN as a direct binding partner of TXNDC5 and a central downstream mediator to regulate ECM homeostasis in ECs. Mutations at Cys89 and Gly351 within the PDI active domains of TXNDC5 markedly disrupted TXNDC5-BGN binding, indicating that PDI activity is essential for this interaction. Consistently, WT-TXNDC5, but not the PDI-inactive mutant, significantly increased FRET efficiency in the BGN folding assay, demonstrating that TXNDC5 facilitates BGN folding in a PDI-dependent manner. This process is critical for BGN maturation, stability, and secretion. Further investigation revealed that BGN was upregulated in the lungs of PH patients and rodent models. Endothelial-specific deficiency of BGN significantly alleviated PH progression in mice, highlighting endothelial-derived BGN as a key contributor to disease pathogenesis. Importantly, BGN deficiency largely abolished TXNDC5 overexpression-induced distal pulmonary arterial remodeling and RV hypertrophy, establishing BGN as a critical downstream effector of TXNDC5-driven PH. Notably, serum BGN levels were significantly elevated in PH patients and strongly correlated with disease severity, suggesting that

BGN may serve as a potential diagnostic biomarker for PH.

Endothelial HIF-2α plays a pivotal role in the pathogenesis of PH[27]. HIF-2α is predominantly localized in ECs and drives sustained transcriptional programs that promote pulmonary vascular remodeling and endothelial dysfunction[28]. In this study, we found that HIF-2α directly binds the promoter region of TXNDC5, driving its transcription. Consistent with previous studies that endothelial loss of prolyl hydroxylase domain protein 2 leads to HIF-2α stabilization and spontaneous PH[29,30], we demonstrated that endothelial-specific overexpression of HIF-2α *in vivo* induced mile PH phenotypes. Notably, these pathological effects were largely abolished in $TXNDC5^{ECKO}$ mice, demonstrating that TXNDC5 is a critical mediator of HIF-2α-driven pulmonary vascular remodeling. Further studies demonstrated that HIF-2α activity was elevated in $TXNDC5^{high}$ ECM-producing ECs. Using a stabilized HIF-2α (dPA) mutant to mimic sustained HIF-2α activation, we demonstrated that HIF-2α is sufficient to transcriptionally induce TXNDC5 and its downstream ECM effectors. Immunofluorescence revealed pronounced deposition of BGN and POSTN in pulmonary arteries upon HIF-2α overexpression, which was markedly attenuated in endothelial TXNDC5-deficient mice. These findings indicate that TXNDC5 acts as a critical downstream effector linking HIF signaling to pathological ECM remodeling, thereby driving pulmonary vascular remodeling and PH development **(Figure 8J)**.

In summary, we identified for the first time the novel role of TXNDC5 in the pathogenesis of PH. Endothelial TXNDC5 functions as a key regulator of ECM homeostasis by promoting the proper folding of BGN. HIF-2α transcriptionally activates TXNDC5, linking hypoxic signaling to pathological ECM accumulation. This study highlights TXNDC5 as a promising therapeutic target for PH and lays the groundwork for future clinical investigations.

Acknowledgments

We thank Professor John Shyy (University of California, San Diego, USA) for critical reading of the manuscript and valuable advice.

Sources of Funding

This work was supported by the Key Program of National Natural Science Foundation of China (grant No. 82430004 to Jin-Song Bian), the National Natural Science Foundation of China (grant No. 82241021 to Xiaowei Nie; grant No. 82400063 to Junting Zhang), Shenzhen Science Fund for Distinguished Young Scholars (grant No. RCJC20210706091946002 to Xiaowei Nie), Shenzhen Science and Technology Program (grant No. GJHZ20240218111401002 to Jin-Song Bian), and the Shenzhen Medical Research Funded Program (Grant No. B2502020 to Jin-Song Bian; Grant No. A2503057 to Junting Zhang).

References

1. Johnson S, Sommer N, Cox-Flaherty K, Weissmann N, Ventetuolo CE, Maron BA. Pulmonary Hypertension: A Contemporary Review. *Am J Respir Crit Care Med*. 2023;208:528–548.

2. Evans CE, Cober ND, Dai Z, Stewart DJ, Zhao Y-Y. Endothelial cells in the pathogenesis of pulmonary arterial hypertension. *Eur Respir J*. 2021;58:2003957.

3. Ma B, Cao Y, Qin J, Chen Z, Hu G, Li Q. Pulmonary artery smooth muscle cell phenotypic switching: A key event in the early stage of pulmonary artery hypertension. *Drug Discov Today*. 2023;28:103559.

4. Mandras SA, Mehta HS, Vaidya A. Pulmonary Hypertension: A Brief Guide for Clinicians. *Mayo Clin Proc*. 2020;95:1978–1988.

5. Olsson KM, Corte TJ, Kamp JC, Montani D, Nathan SD, Neubert L, Price LC, Kiely DG. Pulmonary hypertension associated with lung disease: new insights into pathomechanisms, diagnosis, and management. *Lancet Respir Med*. 2023;11:820–835.

6. Kanemura S, Matsusaki M, Inaba K, Okumura M. PDI Family Members as Guides for Client Folding and Assembly. *Int J Mol Sci*. 2020;21:9351.

7. Kuramochi T, Yamashita Y, Arai K, Kanemura S, Muraoka T, Okumura M. Boosting the enzymatic activity of CxxC motif-containing PDI family members. *Chem Commun (Camb)*. 2024;60:6134–6137.

8. Hung C-T, Tsai Y-W, Wu Y-S, Yeh C-F, Yang K-C. The novel role of ER protein

TXNDC5 in the pathogenesis of organ fibrosis: mechanistic insights and therapeutic implications. *J Biomed Sci*. 2022;29:63.

9. Jin Y, Sharma A, Bai S, Davis C, Liu H, Hopkins D, Barriga K, Rewers M, She J-X. Risk of type 1 diabetes progression in islet autoantibody-positive children can be further stratified using expression patterns of multiple genes implicated in peripheral blood lymphocyte activation and function. *Diabetes*. 2014;63:2506–2515.

10. Wang L, Dong H, Song G, Zhang R, Pan J, Han J. TXNDC5 synergizes with HSC70 to exacerbate the inflammatory phenotype of synovial fibroblasts in rheumatoid arthritis through NF-κB signaling. *Cell Mol Immunol*. 2018;15:685–696.

11. Wang X, Li H, Chang X. The role and mechanism of TXNDC5 in diseases. *Eur J Med Res*. 2022;27:145.

12. Yeh C-F, Cheng S-H, Lin Y-S, Shentu T-P, Huang R-T, Zhu J, Chen Y-T, Kumar S, Lin M-S, Kao H-L, et al. Targeting mechanosensitive endothelial TXNDC5 to stabilize eNOS and reduce atherosclerosis in vivo. *Sci Adv*. 2022;8:eabl8096.

13. Wu S, Luo X, Chen Y, Wang Z, Liu X, Sun N, Zhao J, Luo W, Zhang J, Tong X, et al. Sodium-glucose cotransporter 2 inhibitors attenuate vascular calcification by suppressing endoplasmic reticulum protein thioredoxin domain containing 5 dependent osteogenic reprogramming. *Redox Biol*. 2024;73:103183.

14. Fu Y, Zhou Y, Wang K, Li Z, Kong W. Extracellular Matrix Interactome in Modulating Vascular Homeostasis and Remodeling. *Circ Res*. 2024;134:931–949.

15. Thenappan T, Chan SY, Weir EK. Role of extracellular matrix in the pathogenesis of pulmonary arterial hypertension. *Am J Physiol Heart Circ Physiol*. 2018;315:H1322–H1331.

16. Nie X, Shen C, Tan J, Wu Z, Wang W, Chen Y, Dai Y, Yang X, Ye S, Chen J, et al. Periostin: A Potential Therapeutic Target For Pulmonary Hypertension? *Circ Res*. 2020;127:1138–1152.

17. Bian J-S, Chen J, Zhang J, Tan J, Chen Y, Yang X, Li Y, Deng L, Chen R, Nie X. ErbB3 Governs Endothelial Dysfunction in Hypoxia-Induced Pulmonary Hypertension. *Circulation*. 2024;150:1533–1553.

18. Robinson RM, Reyes L, Duncan RM, Bian H, Reitz AB, Manevich Y, McClure JJ, Champion MM, Chou CJ, Sharik ME, et al. Inhibitors of the protein disulfide isomerase family for the treatment of multiple myeloma. *Leukemia*. 2019;33:1011–1022.

19. Semenza GL. Hypoxia-inducible factors: roles in cardiovascular disease

543 progression, prevention, and treatment. *Cardiovasc Res*. 2023;119:371–380.

544 20. Jiang Q, Braun DA, Clauser KR, Ramesh V, Shirole NH, Duke-Cohan JE, Nabilsi
545 N, Kramer NJ, Forman C, Lippincott IE, et al. HIF regulates multiple translated
546 endogenous retroviruses: Implications for cancer immunotherapy. *Cell*.
547 2025;188:1807-1827.e34.

548 21. Sullivan DC, Huminiecki L, Moore JW, Boyle JJ, Poulsom R, Creamer D, Barker
549 J, Bicknell R. EndoPDI, a novel protein-disulfide isomerase-like protein that is
550 preferentially expressed in endothelial cells acts as a stress survival factor. *J Biol*
551 *Chem*. 2003;278:47079–47088.

552 22. Jandl K, Radic N, Zeder K, Kovacs G, Kwapiszewska G. Pulmonary vascular
553 fibrosis in pulmonary hypertension - The role of the extracellular matrix as a
554 therapeutic target. *Pharmacol Ther*. 2023;247:108438.

555 23. Sun X-J, Ma W-Q, Zhu Y, Liu N-F. POSTN promotes diabetic vascular
556 calcification by interfering with autophagic flux. *Cell Signal*. 2021;83:109983.

557 24. Nikoloudaki G, Snider P, Simmons O, Conway SJ, Hamilton DW. Periostin and
558 matrix stiffness combine to regulate myofibroblast differentiation and fibronectin
559 synthesis during palatal healing. *Matrix Biol*. 2020;94:31–56.

560 25. Yu M, He X, Song X, Gao J, Pan J, Zhou T, Wang Q, Zhu W, Ma H, Zeng H, et al.
561 Biglycan promotes hepatic fibrosis through activating heat shock protein 47. *Liver*
562 *Int*. 2023;43:500–512.

563 26. Appunni S, Rubens M, Ramamoorthy V, Anand V, Khandelwal M, Sharma A.
564 Biglycan: an emerging small leucine-rich proteoglycan (SLRP) marker and its
565 clinicopathological significance. *Mol Cell Biochem*. 2021;476:3935–3950.

566 27. Prchal JT, Gordeuk VR. HIF-2 inhibitor, erythrocytosis, and pulmonary
567 hypertension. *Blood*. 2021;137:2424–2425.

568 28. Shimoda LA. What's HIF Got to Do with It? HIF-2 Inhibition and Pulmonary
569 Hypertension. *Am J Respir Crit Care Med*. 2018;198:1363–1365.

570 29. Dai Z, Li M, Wharton J, Zhu MM, Zhao Y-Y. Prolyl-4 Hydroxylase 2 (PHD2)
571 Deficiency in Endothelial Cells and Hematopoietic Cells Induces Obliterative
572 Vascular Remodeling and Severe Pulmonary Arterial Hypertension in Mice and
573 Humans Through Hypoxia-Inducible Factor-2α. *Circulation*. 2016;133:2447–
574 2458.

575 30. Tang H, Babicheva A, McDermott KM, Gu Y, Ayon RJ, Song S, Wang Z, Gupta
576 A, Zhou T, Sun X, et al. Endothelial HIF-2α contributes to severe pulmonary
577 hypertension due to endothelial-to-mesenchymal transition. *Am J Physiol Lung*
578 *Cell Mol Physiol*. 2018;314:L256–L275.

579 **Figure legends**

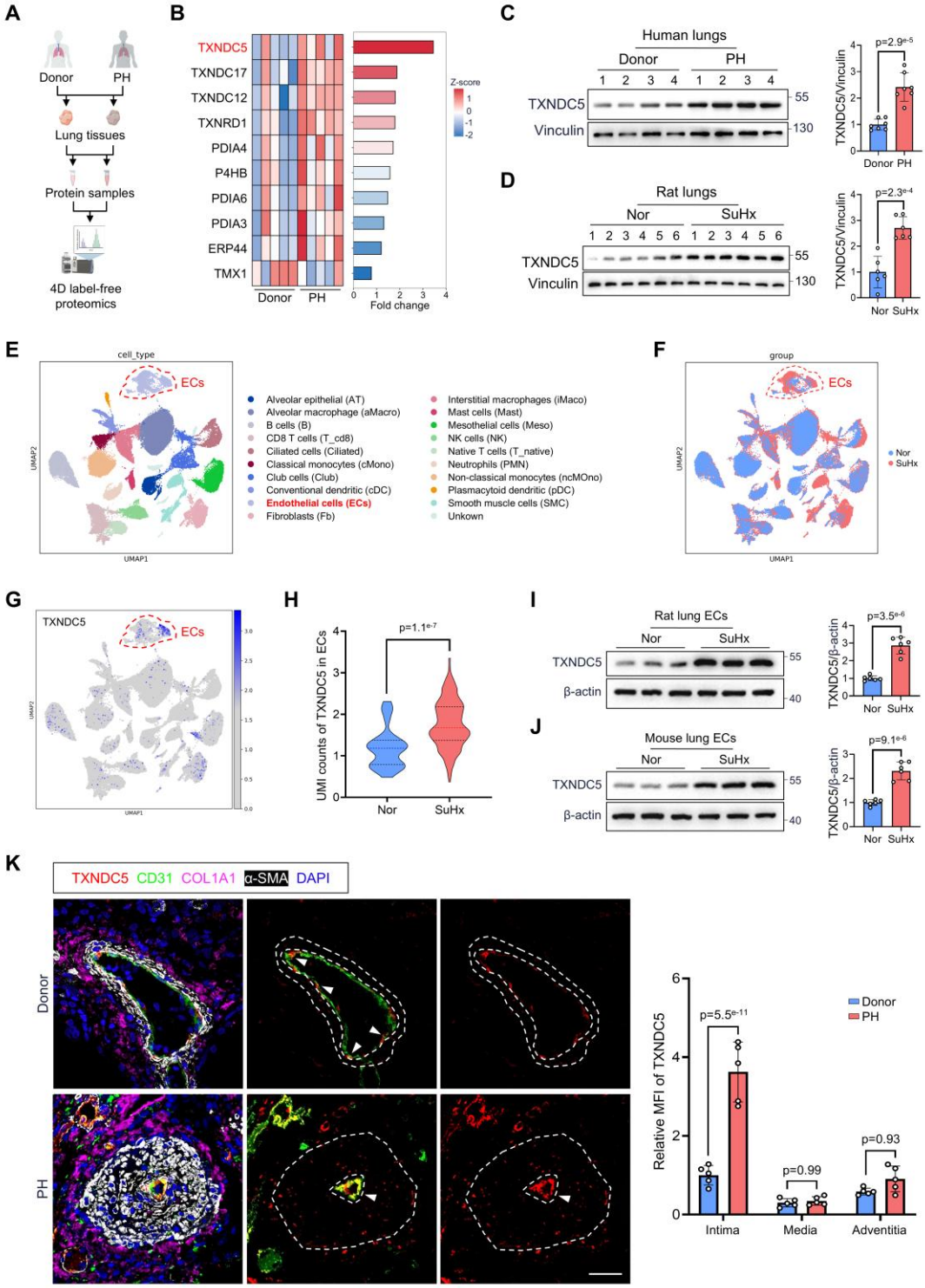

580

581 **Figure 1. TXNDC5 was upregulated in PH.**

582 **A**, Schematic illustration showing the 4D label-free proteomics of lungs from non-PH

583 donors and patients with PH. **B**, Heatmap presenting differential expression of PDI
584 proteins, highlighting TXNDC5 among the members (n=5). **C**, Western blots showing
585 TXNDC5 protein levels in lungs from donors and PH patients (n=7). **D**, Western blots
586 showing TXNDC5 protein levels in lungs from SuHx-treated rats and normoxic
587 controls (Nor) (n=6). **E,** UMAP visualization displaying annotated lung cell types, with
588 endothelial cells (ECs) highlighted. **F,** UMAP plots showing the distribution of lung
589 cell populations from Nor and SuHx-exposed rats. **G**, Feature plot showing TXNDC5
590 expression across lung cell populations. **H**, Violin plot demonstrating TXNDC5
591 expression in ECs quantified by unique molecular identifier (UMI) counts. **I** and **J**,
592 Western blots showing TXNDC5 expression in primary lung ECs from SuHx-treated
593 PH rats and mice compared with controls. **K**, Multiplex immunofluorescence staining
594 showing TXNDC5 (red), CD31 (green), α-SMA (white), and COL1A1 (purple) in
595 pulmonary arteries from human lungs (n=5). Nuclei were counterstained with DAPI
596 (blue). Scale bar=25 μm. MFI indicates mean fluorescence intensity. Data represent the
597 mean±SD. Comparisons of parameters were performed with the unpaired 2-tailed
598 Student *t*-test (**C-D** and **I-J**) or 2-tailed Mann-Whitney *U* test (**H**) or 2-way ANOVA
599 (**K**), followed by Tukey honestly significant difference test for multiple comparisons.
600 PDI indicates protein disulfide isomerase; α-SMA, α-smooth muscle actin; COL1A1,
601 collagen type I alpha 1; DAPI, 4′,6-diamidino-2-phenylindole; Nor, normoxia; and
602 SuHx, Sugen5416/hypoxia.

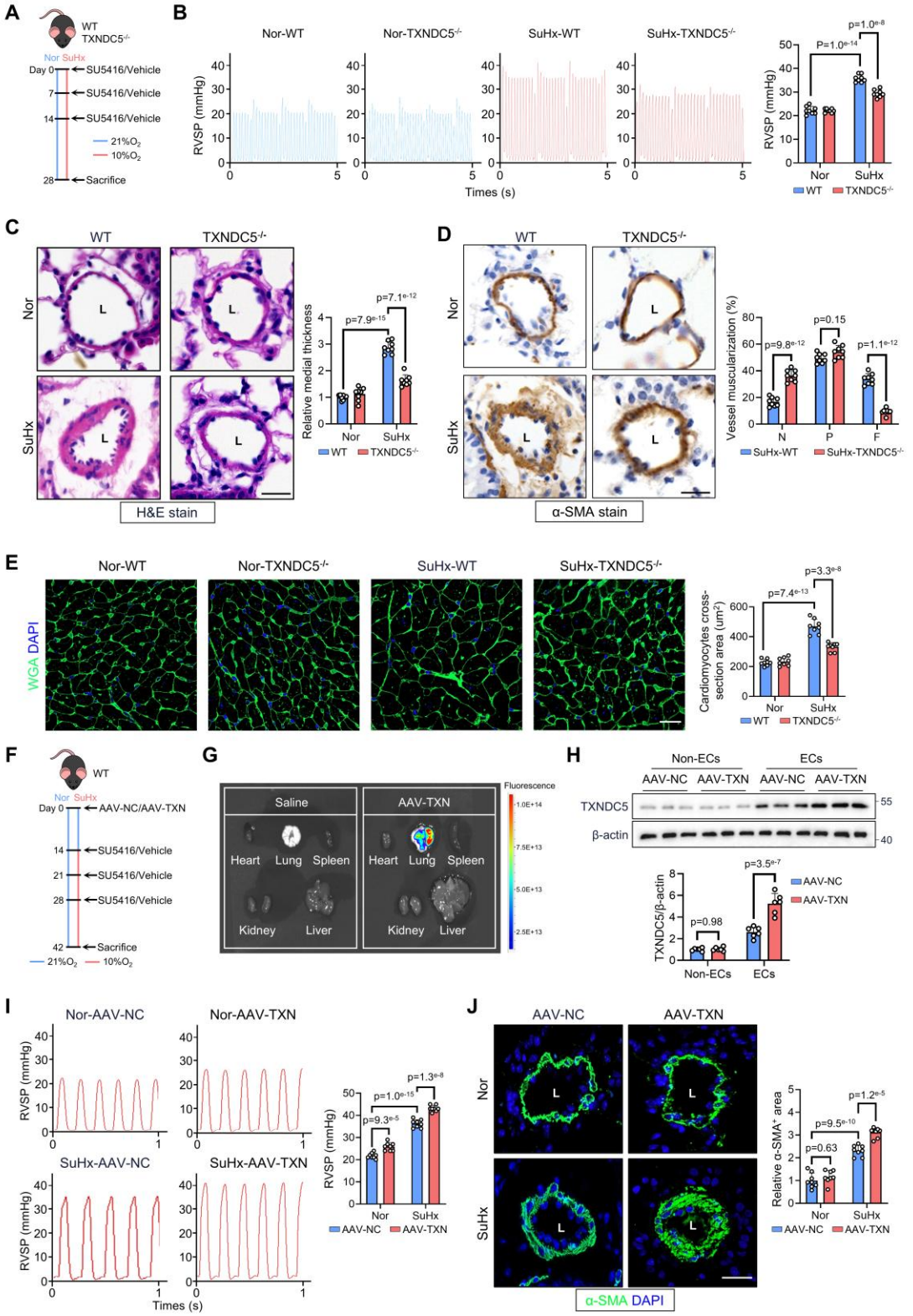

Figure 2. TXNDC5 contributed to SuHx-induced pulmonary vascular remodeling

A, Schematic overview of the SuHx-induced PH protocol in wild-type (WT) or TXNDC5 global knockout (TXNDC5$^{-/-}$) mice. **B**, Hemodynamic measurements showing the tracings and quantification of right ventricular systolic pressure (RVSP) in

608 WT and TXNDC5$^{-/-}$ mice (n=8). **C**, Hematoxylin and eosin (H&E) staining of distal
609 pulmonary arteries in WT and TXNDC5$^{-/-}$ mice (n=8). L indicates lumen. Scale bar=25
610 μm. **D**, Immunohistochemical staining for α-SMA showing the muscularization of
611 distal pulmonary arteries in WT and TXNDC5$^{-/-}$ mice (n=8). L indicates lumen. Scale
612 bar=25 μm. **E**, WGA (green) staining showing the right ventricular morphology in WT
613 and TXNDC5$^{-/-}$ mice (n=8). Nuclei were counterstained with DAPI (blue). Scale
614 bar=20 μm. **F**, Schematic diagram illustrating pulmonary endothelial-specific
615 TXNDC5 overexpression via AAV delivery in mice. **G**, Representative images of major
616 organs from saline-treated control or AAV-TXN-treated mice, lung-targeted
617 fluorescence detected by the IVIS imaging system. **H**, Western blot showing TXNDC5
618 expression in lung endothelial cells (ECs) after AAV delivery (n=6). **I**, Hemodynamic
619 measurements showing RVSP in AAV-TXN- or AAV-NC-treated mice under normoxic
620 or SuHx conditions (n=8). **J**, Immunofluorescence staining for α-SMA displaying the
621 pulmonary arterial smooth muscle coverage in AAV-TXN- or AAV-NC-treated mice.
622 Nuclei were counterstained with DAPI (blue). L indicates lumen. Scale bar=25 μm.
623 Data represent the mean±SD. Comparisons of parameters were performed with 2-way
624 ANOVA, followed by Tukey honestly significant difference test for multiple
625 comparisons. DAPI indicates 4′,6-diamidino-2-phenylindole; α-SMA, α-smooth
626 muscle actin; N, non-muscularized; P, partially muscularized; F, fully muscularized;
627 WGA, wheat germ agglutinin; Nor, normoxia; and SuHx, Sugen5416/hypoxia.

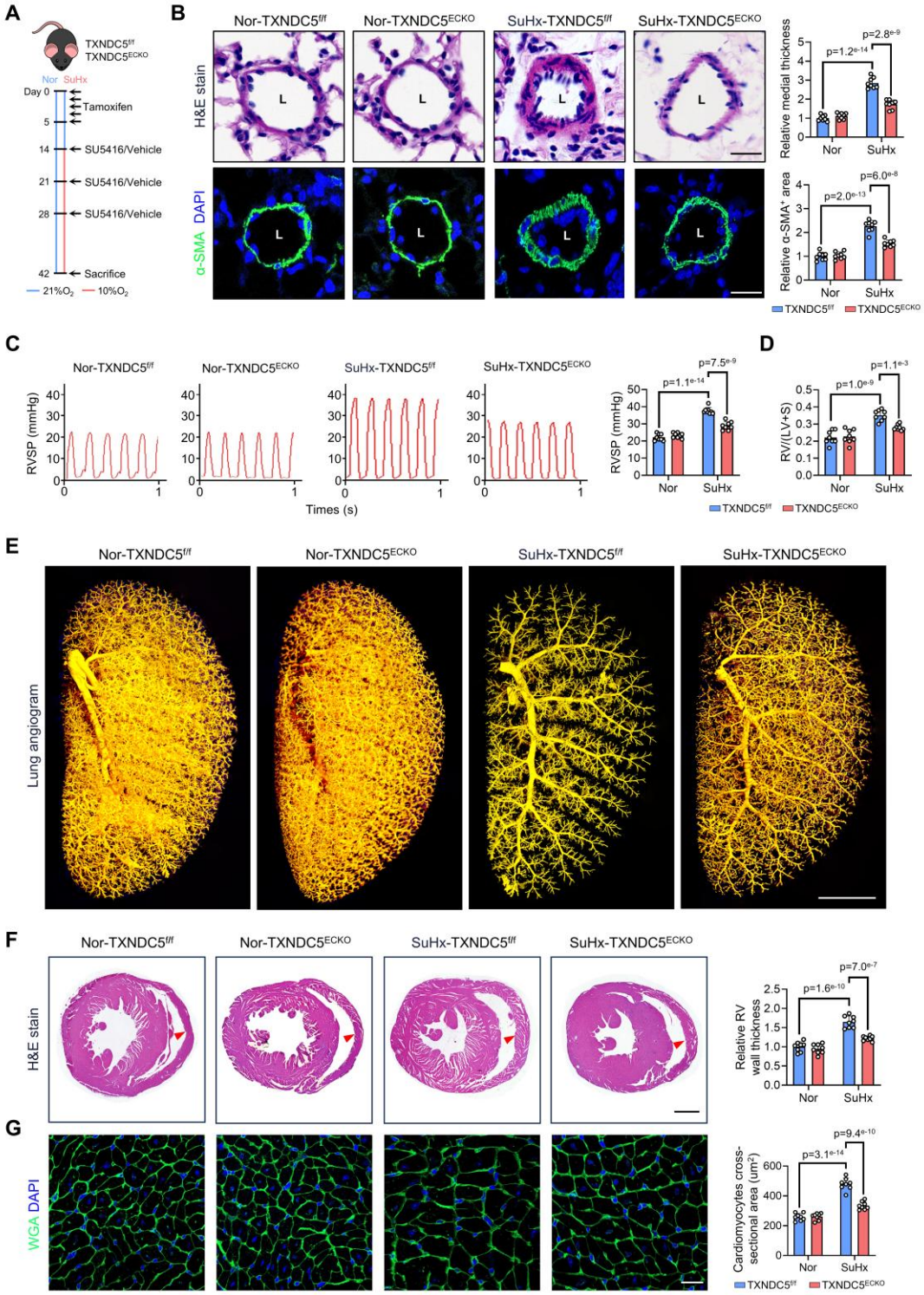

628

629 **Figure 3. Endothelial-specific deletion of TXNDC5 ameliorated SuHx-induced PH.**

630 **A**, Schematic diagram showing the protocol for generating endothelial-specific

631 TXNDC5 knockout (TXNDC5^{ECKO}) mice. **B**, Hematoxylin and eosin (H&E) and α-

632 SMA (green) staining showing distal pulmonary arteries in TXNDC5$^{f/f}$ and

633 TXNDC5^{ECKO} mice under the indicated conditions. Nuclei were counterstained with
634 DAPI (blue). L indicates lumen. Scale bar=25 μm. **C**, Hemodynamic measurements
635 showing the right ventricular systolic pressure (RVSP) in TXNDC5$^{f/f}$ and
636 TXNDC5^{ECKO} mice (n=8). **D**, Fulton index [RV/(LV+S)] demonstrating RV
637 hypertrophy in TXNDC5$^{f/f}$ and TXNDC5^{ECKO} mice (n=8). **E**, Lung angiogram of the
638 left lungs showing intrapulmonary contrast filling in TXNDC5$^{f/f}$ and TXNDC5^{ECKO}
639 mice. Scale bar=2 mm. **F**, Histological cross-sections of the mid-right ventricle
640 showing RV wall morphology in TXNDC5$^{f/f}$ and TXNDC5^{ECKO} mice (n=8). Scale
641 bar=1 mm. **G**, Immunofluorescence staining of WGA (green) showing right ventricular
642 cardiomyocyte hypertrophy in TXNDC5$^{f/f}$ and TXNDC5^{ECKO} mice. Nuclei were
643 counterstained with DAPI (blue). Scale bar=20 μm. Data represent the mean±SD.
644 Comparisons of parameters were performed with 2-way ANOVA, followed by Tukey
645 honestly significant difference test for multiple comparisons. DAPI indicates 4′,6-
646 diamidino-2-phenylindole; α-SMA, α-smooth muscle actin; WGA, wheat germ
647 agglutinin; f/f, flox/flox; Nor, normoxia; SuHx, Sugen5416/hypoxia; and RV, right
648 ventricular.

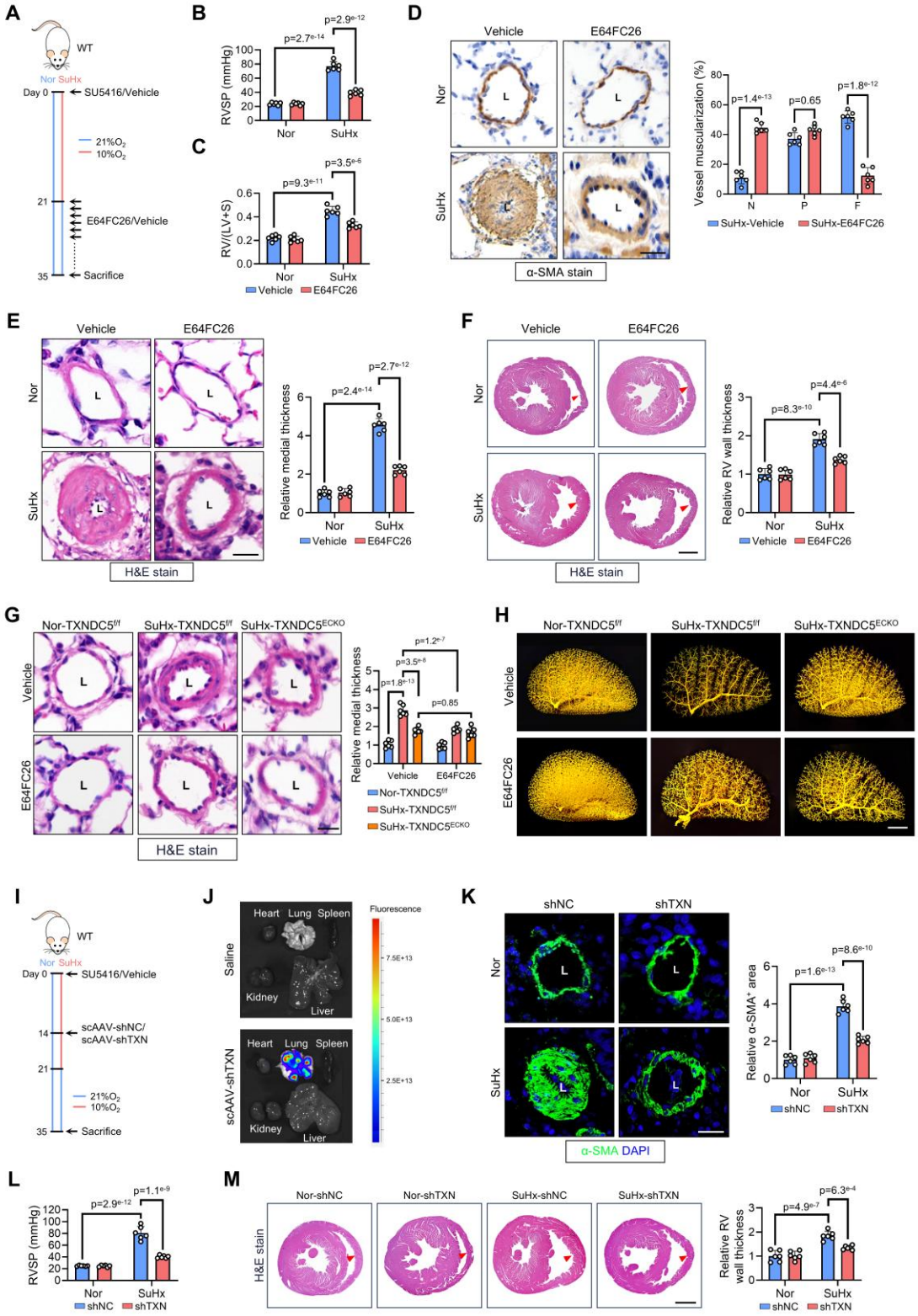

649

650 **Figure 4. Pharmacological and pulmonary endothelium-targeted inhibition of**
651 **TXNDC5 ameliorated PH.**

652 **A**, Schematic showing the E64FC26 treatment protocol in SuHx-induced PH rats. **B**,
653 Hemodynamic measurements showing right ventricular systolic pressure (RVSP) in

654 vehicle- or E64FC26-treated rats (n=6). **C**, Fulton index [RV/(LV+S)] in rats treated
655 with vehicle or E64FC26 (n=6). **D**, Immunohistochemical staining for α-SMA showing
656 muscularization of distal pulmonary arteries in vehicle- or E64FC26-treated rats (n=6).
657 L indicates lumen. Scale bar=25 μm. **E**, Hematoxylin and eosin (H&E) staining
658 showing distal pulmonary arterial morphology in vehicle- or E64FC26-treated rats
659 (n=6). L indicates lumen. Scale bar=25 μm. **F**, Histological sections of mid-right
660 ventricle showing RV wall thickening in vehicle- or E64FC26-treated rats (n=6). Scale
661 bar=2 mm. **G**, H&E staining showing distal pulmonary arterial morphology in
662 $TXNDC5^{f/f}$ and $TXNDC5^{ECKO}$ mice treated with vehicle or E64FC26 (n=6). L indicates
663 lumen. Scale bar=25 μm. **H**, Lung angiography images showing distal pulmonary
664 perfusion. Scale bar=2 mm. **I**, Schematic showing pulmonary endothelium-targeted
665 gene therapy using self-complementary adeno-associated virus (scAAV) encoding
666 shRNA against TXNDC5 (shTXN) or control shRNA (shNC). **J**, IVIS imaging showing
667 lung fluorescence signals in scAAV-treated rats. **K**, Immunofluorescence staining
668 showing α-SMA (green) positive area in distal pulmonary arteries in shNC- or shTXN-
669 treated rats (n=6). Nuclei were counterstained with DAPI (blue). L indicates lumen.
670 Scale bar=25 μm. **L**, Hemodynamic measurements showing RVSP in shNC- or shTXN-
671 treated rats (n=6). **M**, H&E staining of mid-right ventricle sections showing RV wall
672 morphology in shNC- or shTXN-treated rats (n=6). Scale bar=2 mm. Data represent the
673 mean±SD. Comparisons of parameters were performed with 2-way ANOVA, followed
674 by Tukey honestly significant difference test for multiple comparisons.α-SMA indicates
675 α-smooth muscle actin; N, non-muscularized; P, partially muscularized; F, fully
676 muscularized; shRNA, short hairpin RNA; f/f, flox/flox; Nor, normoxia; SuHx,
677 Sugen5416/hypoxia; and RV, right ventricular.

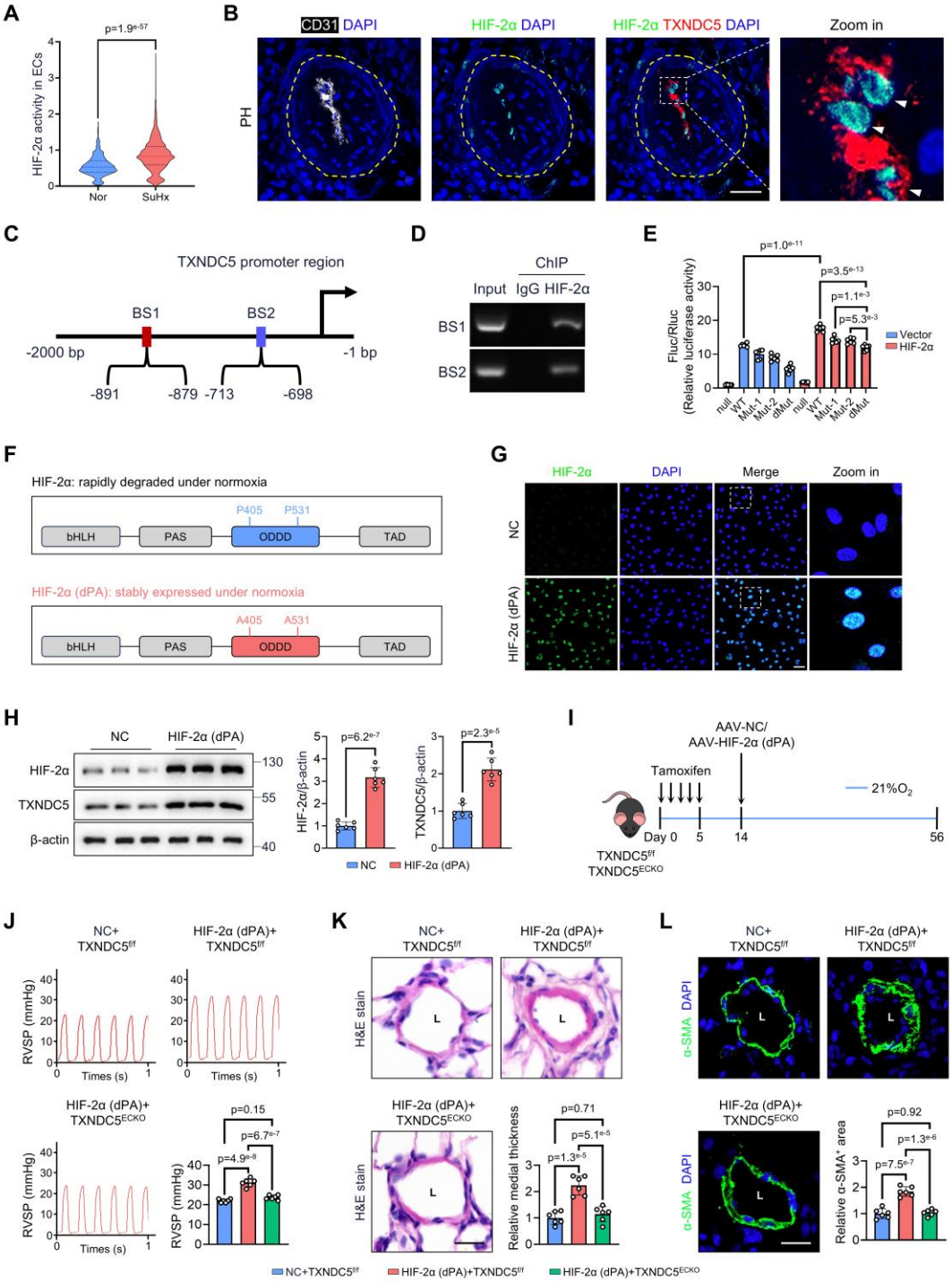

Figure 5. HIF-2α transcriptionally activated TXNDC5 to drive PH.

A, Single-cell RNA sequencing analysis showing HIF-2α activity inferred from the expression of its target genes in endothelial cells (ECs) from normoxic (Nor) and SuHx-treated rat lungs. **B**, Immunofluorescence staining of pulmonary arteries from patients

683 with PH showing CD31 (white), HIF-2α (green), and TXNDC5 (red). Nuclei were
684 counterstained with DAPI (blue). Scale bar=25 μm. **C**, Schematic illustration showing
685 two putative HIF-2α binding sites (BS1 and BS2) in the TXNDC5 promoter region. **D**,
686 Chromatin immunoprecipitation (ChIP) followed by polymerase chain reaction
687 analysis showing HIF-2α binding to the BS1 and BS2 regions of the TXNDC5 promoter.
688 **E**, Dual-luciferase reporter assay showing TXNDC5 promoter activity with mutation
689 of the HIF-2α binding sites [Mut-1, Mut-2, or double mutant (dMut)] (n=6). **F**,
690 Schematic of HIF-2α (dPA) mutant harboring double Pro405Ala/Pro531Ala
691 substitutions that enable stable expression under normoxia. **G**, Immunofluorescence
692 staining showing HIF-2α (green) in PAECs after lentiviral delivery of HIF-2α (dPA).
693 Nuclei were counterstained with DAPI (blue). Scale bar=50 μm. **H**, Western blot
694 analysis showing HIF-2α and TXNDC5 expression in PAECs after HIF-2α
695 overexpression (n=6). **I**, Schematic showing the experimental design for endothelial-
696 specific overexpression of HIF-2α (dPA) in $TXNDC5^{f/f}$ and $TXNDC5^{ECKO}$ mice. **J**,
697 Hemodynamic measurements showing right ventricular systolic pressure (RVSP) in
698 $TXNDC5^{f/f}$ and $TXNDC5^{ECKO}$ mice after endothelial HIF-2α overexpression (n=6). **K**,
699 Hematoxylin and eosin (H&E) staining showing distal pulmonary arterial morphology
700 in $TXNDC5^{f/f}$ and $TXNDC5^{ECKO}$ mice (n=6). L indicates lumen. Scale bar=25 μm. **L**,
701 Immunofluorescence staining for α-SMA (green) showing the α-SMA-positive area in
702 pulmonary arteries. Nuclei were counterstained with DAPI (blue). L indicates lumen.
703 Scale bar=25 μm. Data represent the mean±SD. Comparisons of parameters were
704 performed with the 2-tailed Mann-Whitney *U* test (**A**) or unpaired 2-tailed Student *t*-
705 test (**H**) or 1-way (**J-L**) or 2-way (**E**) ANOVA, followed by the Tukey honestly
706 significant difference test for multiple comparisons. Nor indicates normoxia; NC,
707 negative control; α-SMA, α-smooth muscle actin; bHLH, basic helix-loop-helix; PAS,
708 Per-Arnt-Sim motifs; ODDD, oxygen-dependent degradation domain; and TAD,
709 transcriptional activation domain.

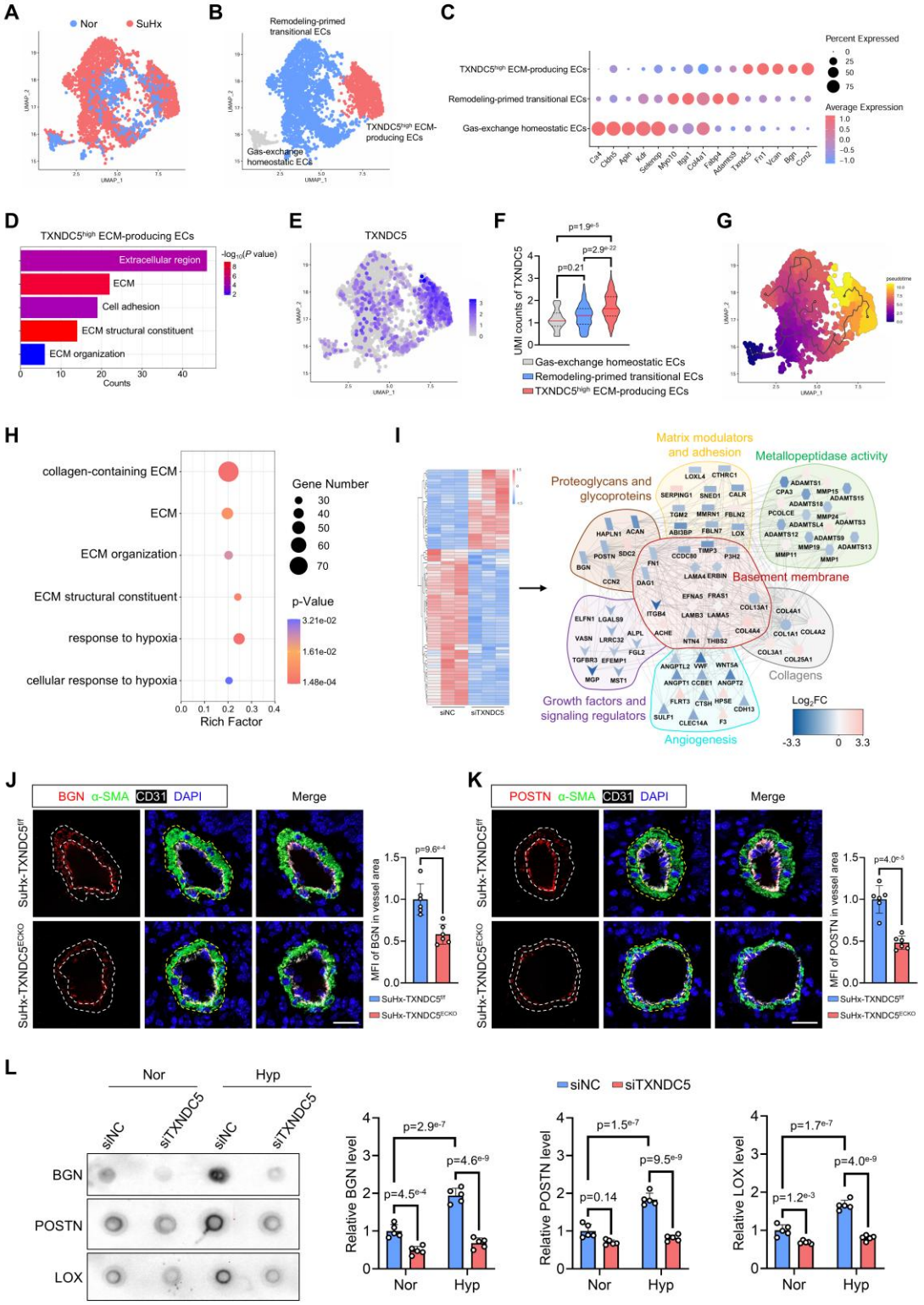

Figure 6. TXNDC5 regulated ECM protein expression and deposition.

A and **B**, Reclustering analysis of endothelial cells (ECs) from the single-cell RNA-seq dataset, showing three transcriptionally distinct subpopulations in UMAP plots with cluster distribution. **C**, Dot plot showing representative markers for each endothelial

population. **D**, Gene ontology enrichment analysis showing the top 200 marker genes in TXNDC5^{high} ECM-producing ECs. **E**, UMAP feature plot showing the distribution of TXNDC5 expression across distinct endothelial clusters. **F,** Quantitative analysis of unique molecular identifier (UMI) counts showing TXNDC5 expression across the three endothelial subpopulations. **G**, Pseudotime trajectory analysis showing the inferred transitional relationship among cell states. **H**, Bubble chart showing the Gene ontology analysis of bulk RNA sequencing data from PAECs transfected with siTXNDC5 or siNC under hypoxia exposure (n=3). **I**, Heatmap showing differentially expressed ECM proteins, together with a PPI network showing functional subgroup classification of the ECM proteins. **J** and **K**, Immunofluorescence staining showing biglycan (BGN) and periostin (POSTN) deposition in pulmonary arteries from TXNDC5$^{f/f}$ and TXNDC5^{ECKO} mice after SuHx exposure (n=6). Nuclei were counterstained with DAPI (blue). Scale bar=25 μm. MFI indicates mean fluorescence intensity. **L**, Dot blot analysis showing BGN, POSTN, and lysyl oxidase (LOX) in supernatants from PAECs (n=5). Data represent the mean±SD. Comparisons of parameters were performed with the unpaired 2-tailed Student *t*-test (**J** and **K**) or 1-way (**F**) or 2-way ANOVA (**L**), followed by Tukey honestly significant difference test for multiple comparisons. ECM indicates extracellular matrix; PPI, protein-protein interaction; Nor, normoxia; Hyp, hypoxia; SuHx, Sugen5416/hypoxia; si, small interfering; and α-SMA, α-smooth muscle actin.

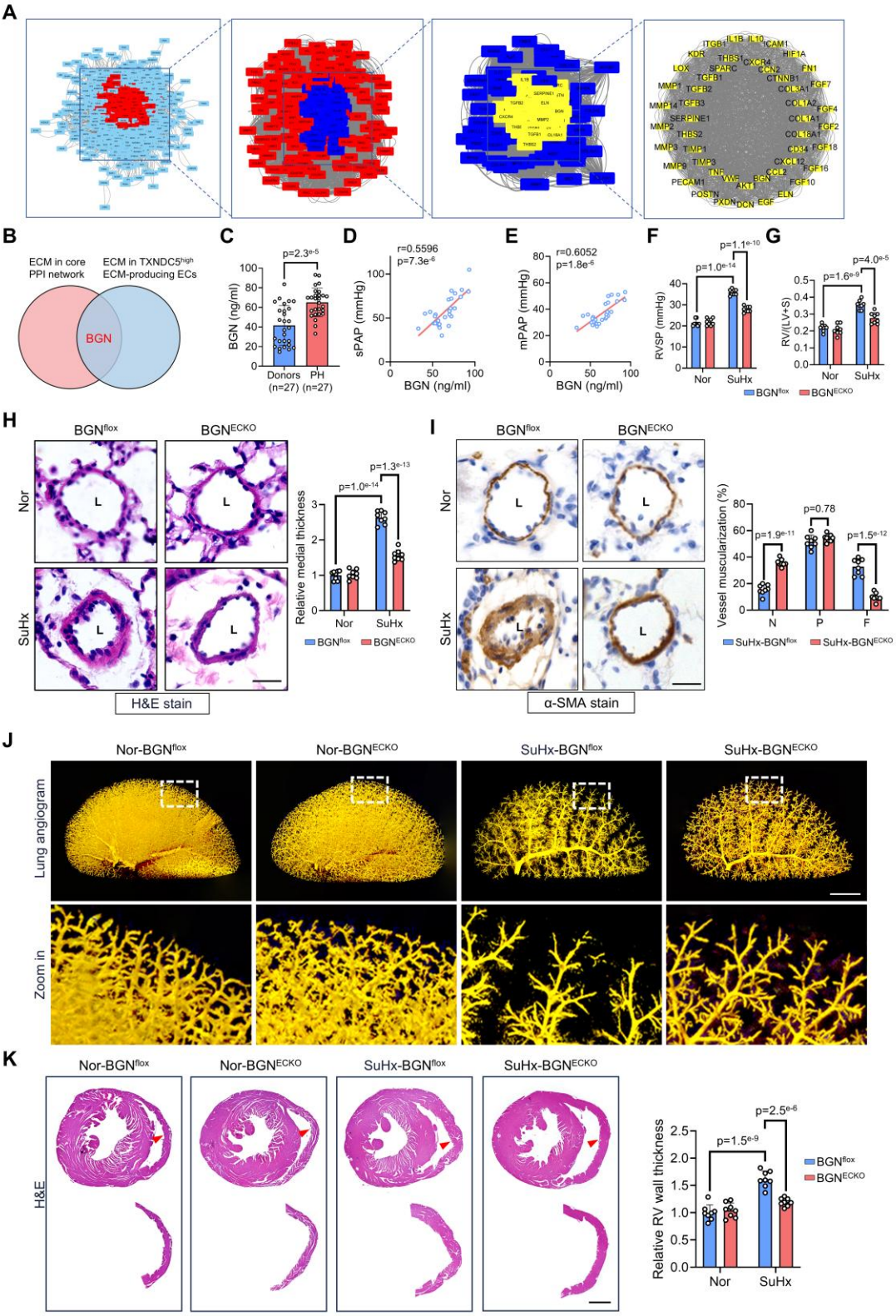

Figure 7. BGN served as a biomarker and therapeutic target of PH.

A, Progressive PPI network analysis showing interaction between ECM genes and endothelial function-related genes, with each network building on the core genes of the previous one. **B**, Venn diagram illustrating the overlap between ECM proteins in the

740 final core PPI network and ECM proteins enriched in TXNDC5^{high} ECM-producing
741 ECs. **C,** Enzyme-linked immunosorbent assay showing the serum BGN concentrations
742 in PH patients and non-PH donors (n=27 per group). **D-E**, Linear regression analysis
743 showing the correalation between serum BGN levels and sPAP or mPAP in PH patients
744 (n=27). **F**, Hemodynamic measurements showing right ventricular systolic pressure
745 (RVSP) in BGN^{flox} and BGN^{ECKO} mice under the indicated conditions (n=8). **G**, Fulton
746 index [RV/(LV+S)] in BGN^{flox} and BGN^{ECKO} mice (n=8). **H**, Hematoxylin and eosin
747 (H&E) staining showing distal pulmonary arterial morphology in BGN^{flox} and
748 BGN^{ECKO} mice. L indicates lumen. Scale bar=25 μm. **I**, Immunohistochemical staining
749 for α-SMA showing muscularization of pulmonary arteries (n=8). L indicates lumen.
750 Scale bar=25 μm. **J**, Lung angiogram displaying distal pulmonary vascular filling in
751 BGN^{flox} and BGN^{ECKO} mice. Scale bar=2 mm. **K**, H&E staining of mid-right ventricle
752 sections showing RV wall thickening in BGN^{flox} and BGN^{ECKO} mice (n=8). Scale bar=
753 1 mm. Data represent the mean±SD. Comparisons of parameters were performed with
754 the 2-tailed Mann-Whitney *U* test (**C**), Pearson correlation test (**D** and **E**), or 2-way
755 ANOVA (**F-I**, and **K**), followed by Tukey honestly significant difference test for
756 multiple comparisons. α-SMA indicates α-smooth muscle actin; DAPI, 4′,6-diamidino-
757 2-phenylindole; Nor, normoxia; SuHx, Sugen5416/hypoxia; N, non-muscularized; P,
758 partially muscularized; F, fully muscularized; RV, right ventricular; sPAP, systolic
759 pulmonary arterial pressure; and mPAP, mean pulmonary arterial pressure.

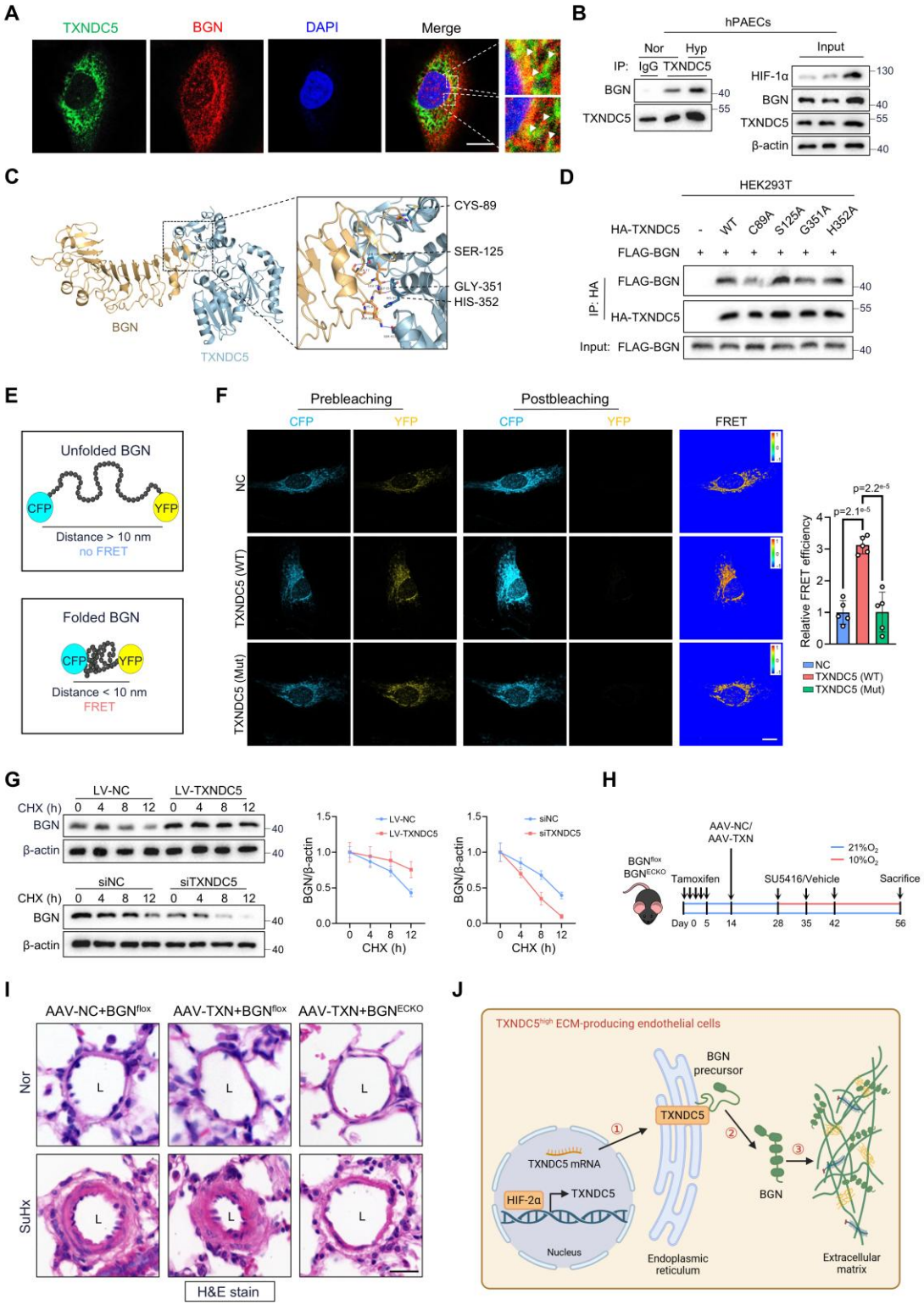

760

761 **Figure 8. TXNDC5 assisted BGN protein folding to promote PH.**

762 **A**, Immunofluorescence staining showing TXNDC5 (green) and BGN (red)
763 localization in PAECs. Nuclei were stained with DAPI (blue). Scale bar=10 μm. **B**,
764 Coimmunoprecipitation (co-IP) analysis showing the interaction between TXNDC5

765 and BGN in PAECs under both normoxic and hypoxic situations. IgG was used as the
766 negative control. **C**, Molecular docking showing the interaction sites between TXNDC5
767 and BGN, highlighting Cys89, Ser125, Gly351, and His352 residues of TXNDC5. **D**,
768 Immunoprecipitation with anti-HA beads in HEK293T cells transfected with FLAG-
769 BGN and HA-TXNDC5 mutant plasmids. **E**, Schematic illustration showing the FRET-
770 based assay used to assess BGN protein folding in PAECs. When the BGN protein folds
771 correctly (bottom), the distance between CFP and YFP will be less than 10 nm, resulting
772 in FRET occurring. **F**, FRET-based protein folding assays demonstrating BGN folding
773 efficiency in PAECs expressing wild-type TXNDC5 (TXNDC5 WT) or PDI-inactive
774 TXNDC5 mutant (TXNDC5 Mut) (n=5). Scale bar=10 μm. **G**, Cycloheximide (CHX)
775 chase assays showing BGN protein stability in PAECs with TXNDC5 overexpression
776 or silencing (n=6). **H**, Schematic showing the experimental design for endothelial-
777 specific TXNDC5 overexpression in BGN^{flox} and BGN^{ECKO} mice under SuHx exposure.
778 **I**, Hematoxylin and eosin (H&E) staining showing distal pulmonary arterial
779 morphology in BGN^{flox} and BGN^{ECKO} mice under indicated conditions (n=6). L
780 indicates lumen. Scale bar=25 μm. **J**, Schematic illustration of the HIF-2α-TXNDC5-
781 BGN axis regulating ECM remodeling in $TXNDC5^{high}$ ECM-producing endothelial
782 cells during PH development. Data represent the mean±SD. Comparisons of parameters
783 were performed with the 1-way (**F**) or 2-way (**G**) ANOVA, followed by the Tukey
784 honestly significant difference test for multiple comparisons. Nor indicates normoxia;
785 Hyp, hypoxia; IgG, immunoglobulin G; FRET, fluorescence resonance energy transfer;
786 CFP, cyan fluorescent protein; and YFP, yellow fluorescent protein.
787

Supplemental Figures

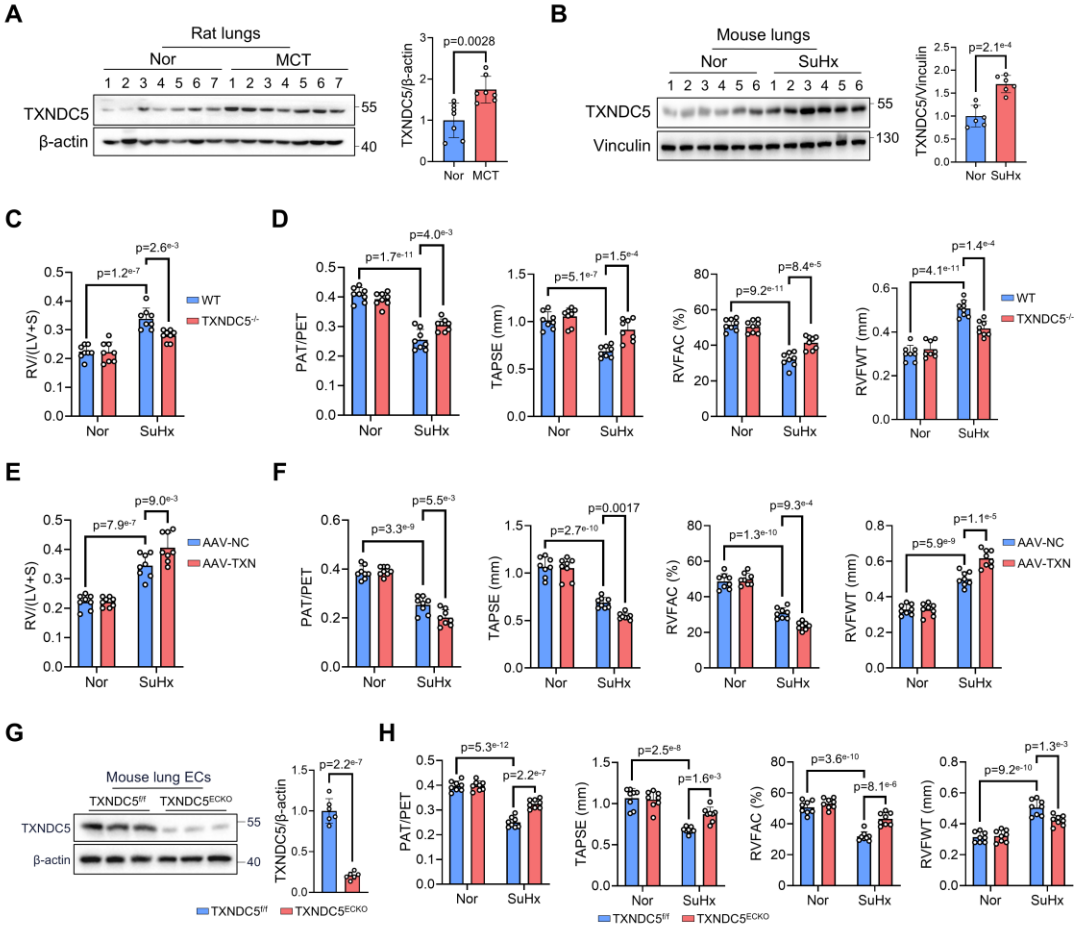

Figure S1. Endothelial TXNDC5 was upregulated and associated with pulmonary vascular remodeling in PH.

A, Western blot analysis and quantification showing TXNDC5 protein levels in lungs

793 from monocrotaline (MCT)-treated rats and controls (n=7). **B**, Western blot analysis
794 showing TXNDC5 protein levels in lungs from SuHx-exposed mice and normoxic
795 controls (n=6). **C**, Fulton index [RV/(LV+S)] in WT and TXNDC5$^{-/-}$ mice (n=8). **D**,
796 Echocardiography analysis showing right ventricular function parameters in WT and
797 TXNDC5$^{-/-}$ mice (n=8). **E**, RV/(LV+S) in mice receiving pulmonary endothelial
798 TXNDC5 overexpression (AAV-TXN) or control (AAV-NC) (n=8). **F**,
799 Echocardiography analysis showing right ventricular function parameters in AAV-
800 TXN- or AAV-NC-treated mice (n=8). **G**, Western blot analysis showing TXNDC5
801 expression in lung endothelial cells (ECs) from TXNDC5^{ECKO} and control mice (n=6).
802 **H**, Echocardiography analysis showing right ventricular function parameters in
803 TXNDC5^{ECKO} mice and TXNDC5$^{f/f}$ controls (n=8). Data represent the mean±SD.
804 Comparisons of parameters were performed with the unpaired 2-tailed Student *t*-test
805 (**A-B** and **G**) or 2-way ANOVA (**C-F**, and **H**), followed by Tukey honestly significant
806 difference test for multiple comparisons. Nor indicates normoxia; SuHx,
807 Sugen5416/hypoxia; and f/f, flox/flox.

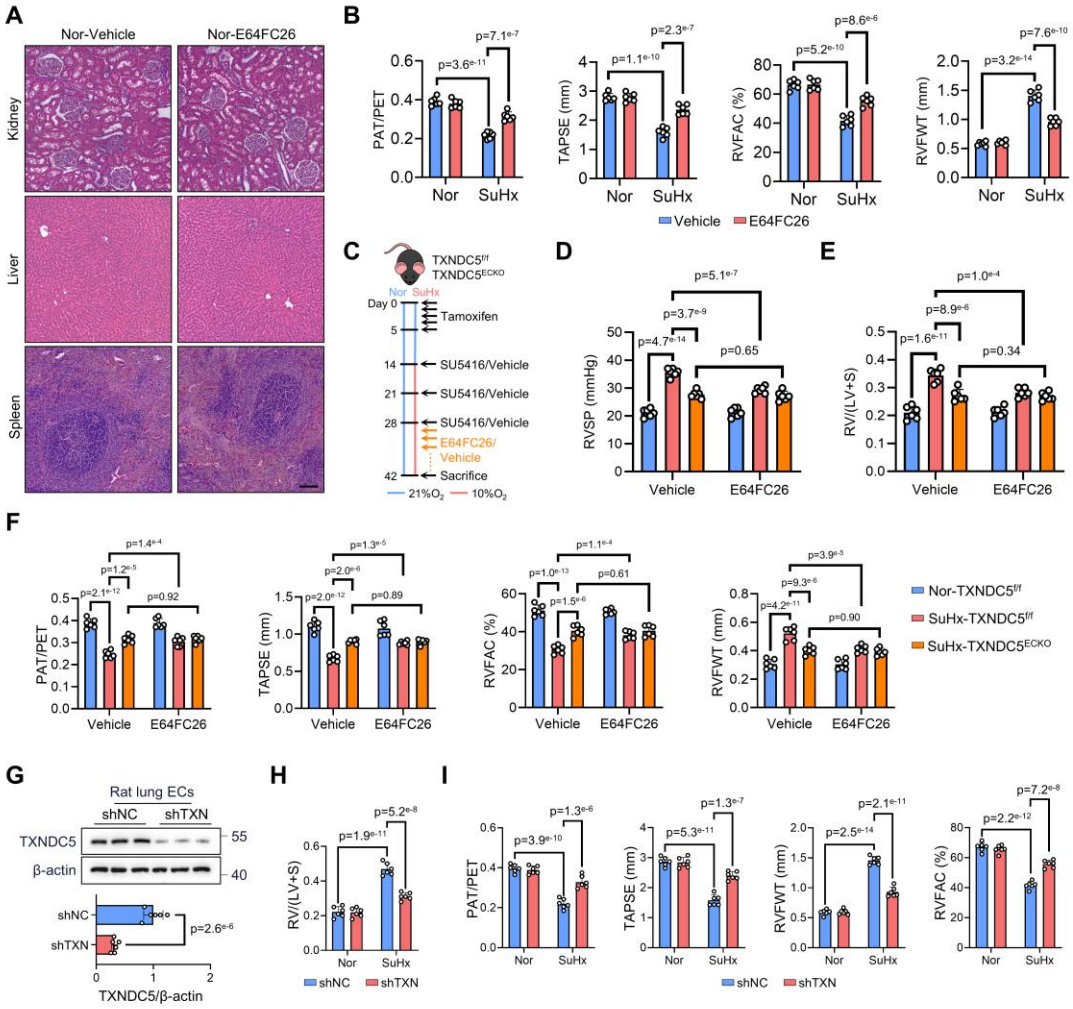

Figure S2. TXNDC5 inhibition showed therapeutic efficacy in PH.

A, Hematoxylin and eosin (H&E) staining showing kidney, liver, and spleen morphology in normoxic rats treated with E64FC26 or vehicle for 5 weeks. Scale bar=100 μm. **B**, Echocardiography demonstrated improved RV function with E64FC26

813 treatment (n=6). **C**, Schematic illustrating vehicle or E64FC26 treatment in TXNDC5$^{f/f}$
814 and TXNDC5^{ECKO} mice. **D-E**, Hemodynamic and morphometric measurements
815 showing right ventricular systolic pressure (RVSP) and the Fulton index [RV/(LV+S)]
816 in TXNDC5$^{f/f}$ and TXNDC5^{ECKO} mice treated with E64FC26 or vehicle (n=6). **F**,
817 Echocardiography analysis showing RV function parameters in TXNDC5$^{f/f}$ and
818 TXNDC5^{ECKO} mice under the indicated conditions (n=6). **G**, Western blot showing
819 TXNDC5 expression in lung endothelial cells (ECs) isolated from rats receiving
820 pulmonary endothelium-targeted self-complementary adeno-associated virus (scAAV)
821 carrying shRNA against TXNDC5 (shTXN) or control shRNA (shNC) (n=6). **H-I**,
822 RV/(LV+S) and echocardiographic RV function parameters in shNC- or shTXN-treated
823 rats (n=6). Data represent the mean±SD. Comparisons of parameters were performed
824 with the unpaired 2-tailed Student *t*-test (**G**) or 2-way ANOVA (**B**, **D-F**, and **H-I**),
825 followed by Tukey honestly significant difference test for multiple comparisons. f/f
826 indicates flox/flox; Nor, normoxia; SuHx, Sugen5416/hypoxia; RV, right ventricular;
827 and shRNA, short hairpin RNA.

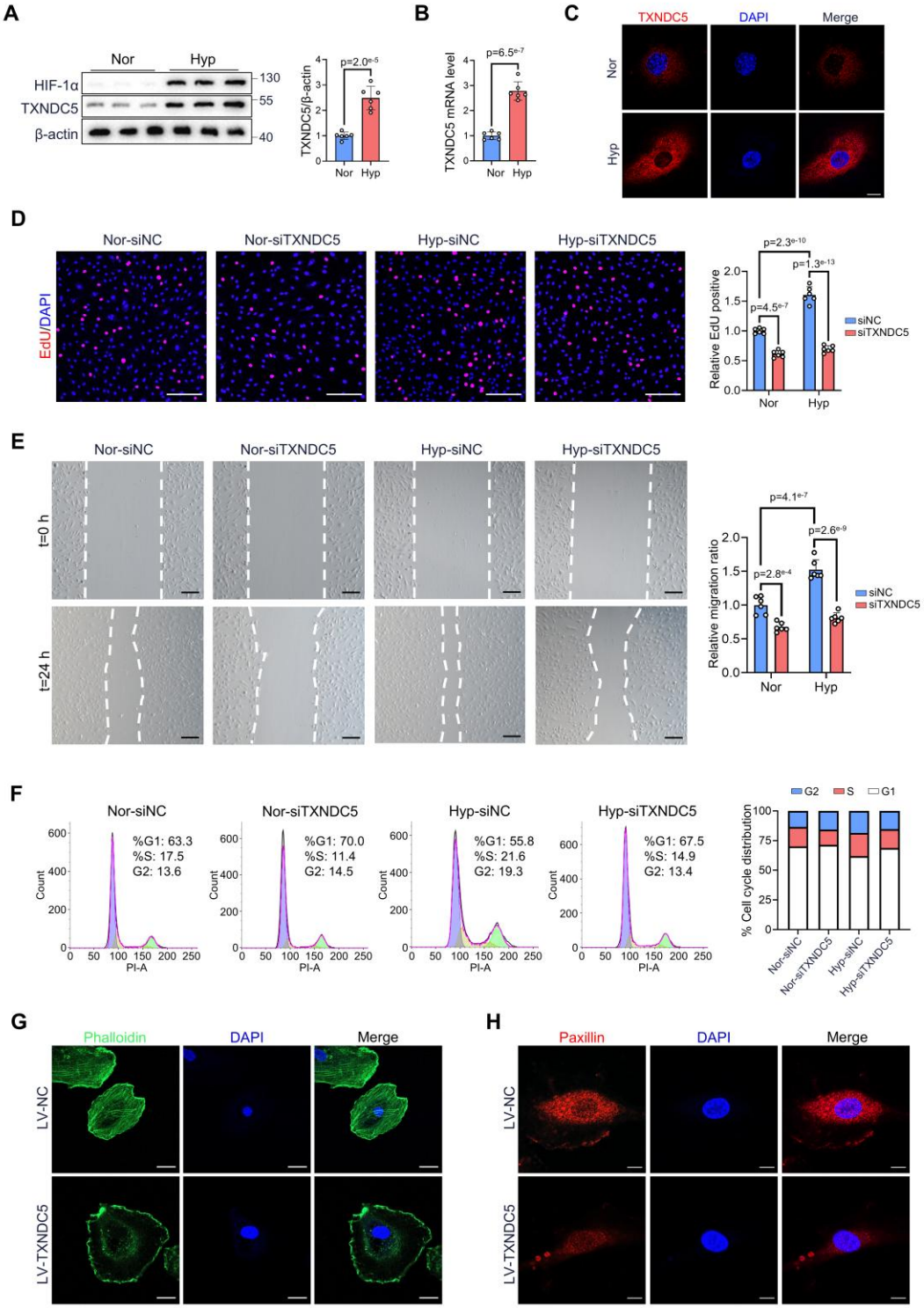

Figure S3. TXNDC5 regulated pulmonary arterial endothelial cell function.

A and **B**, Western blot and qPCR analyses showing TXNDC5 expression levels in PAECs under normoxia and hypoxia (n=6). **C**, Immunofluorescence staining showing TXNDC5 expression and subcellular localization. Scale bar=10 μm. **D**, Representative

833 EdU staining images and quantification showing PAECs proliferation after TXNDC5
834 silencing (n=6). Nuclei were counterstained with DAPI (blue). Scale bar=200 μm. **E**,
835 Representative images and group data showing PAECs migration after TXNDC5
836 silencing under normoxia and hypoxia (n=6). Scale bar=200 μm. **F**, Flow cytometry
837 analysis showing cell cycle distribution in PAECs after TXNDC5 silencing (n=6). **G**
838 and **H**, Immunofluorescence staining showing cytoskeletal organization in PAECs after
839 TXNDC5 overexpression via lentivirus (LV-TXNDC5). Phalloidin (green, scale bar=20
840 μm) and paxillin (red, scale bar=10 μm) staining were used. Nuclei were counterstained
841 with DAPI (blue). Data represent the mean±SD. Comparisons of parameters were
842 performed with the unpaired 2-tailed Student *t*-test (**A** and **B**) or 2-way ANOVA (**D** and
843 **E**), followed by Tukey honestly significant difference test for multiple comparisons.
844 Nor indicates normoxia; Hyp, hypoxia; si, small interfering; qPCR, quantitative
845 polymerase chain reaction; and EdU, 5-ethynyl-20-deoxyuridine.

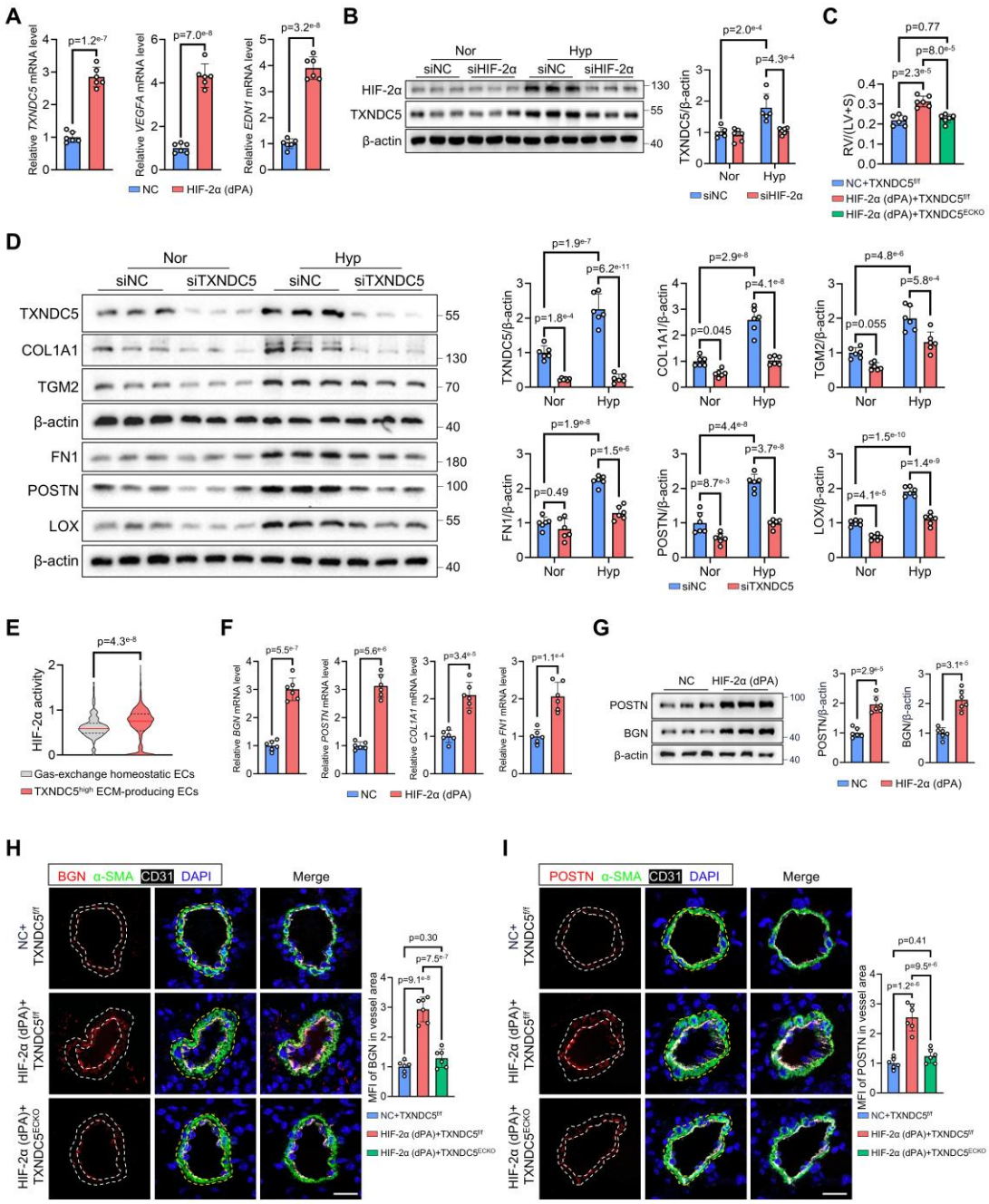

Figure S4. **TXNDC5 was required for HIF-2a-driven ECM remodeling.**

A, Quantitative polymerase chain reaction (qPCR) analysis showing mRNA levels of TXNDC5, VEGFA, and EDN1 in PAECs following HIF-2α (dPA) overexpression (n=6). **B**, Western blot analysis showing TXNDC5 protein levels in PAECs under

851 hypoxia with or without HIF-2α silencing (n=6). **C**, Fulton index [RV/(LV+S)] in
852 TXNDC5$^{f/f}$ and TXNDC5^{ECKO} mice after endothelial HIF-2α overexpression (n=6). **D**,
853 Western blot showing ECM protein expression, including COL1A1, TGM2, FN1,
854 POSTN, and LOX, in PAECs following TXNDC5 silencing with or without hypoxia
855 exposure (n=6). **E**, Single-cell RNA-sequencing analysis showing HIF-2α activity in
856 Gas-exchange homeostatic ECs and TXNDC5^{high} ECM-producing ECs. **F**, qPCR
857 showing the mRNA levels of representative ECM genes, including BGN, POSTN,
858 COL1A1, and FN1 in PAECs after HIF-2α overexpression (n=6). **G**, Western blot
859 showing POSTN and BGN protein levels in PAECs (n=6). **H** and **I,**
860 Immunofluorescence staining showing BGN and POSTN in pulmonary arteries of
861 TXNDC5$^{f/f}$ and TXNDC5^{ECKO} mice after endothelial HIF-2α (dPA) overexpression
862 (n=6). Data represent the mean±SD. Comparisons of parameters were performed with
863 the unpaired 2-tailed Student *t*-test (**A, F, and G**) or 2-tailed Mann-Whitney *U* test (**E**)
864 or one- way (**C**, **H,** and **I**) or 2-way ANOVA (**D**), followed by Tukey honestly
865 significant difference test for multiple comparisons. Nor indicates normoxia; Hyp,
866 hypoxia; SuHx, Sugen5416/hypoxia; si, small interfering; and ECs, endothelial cells.

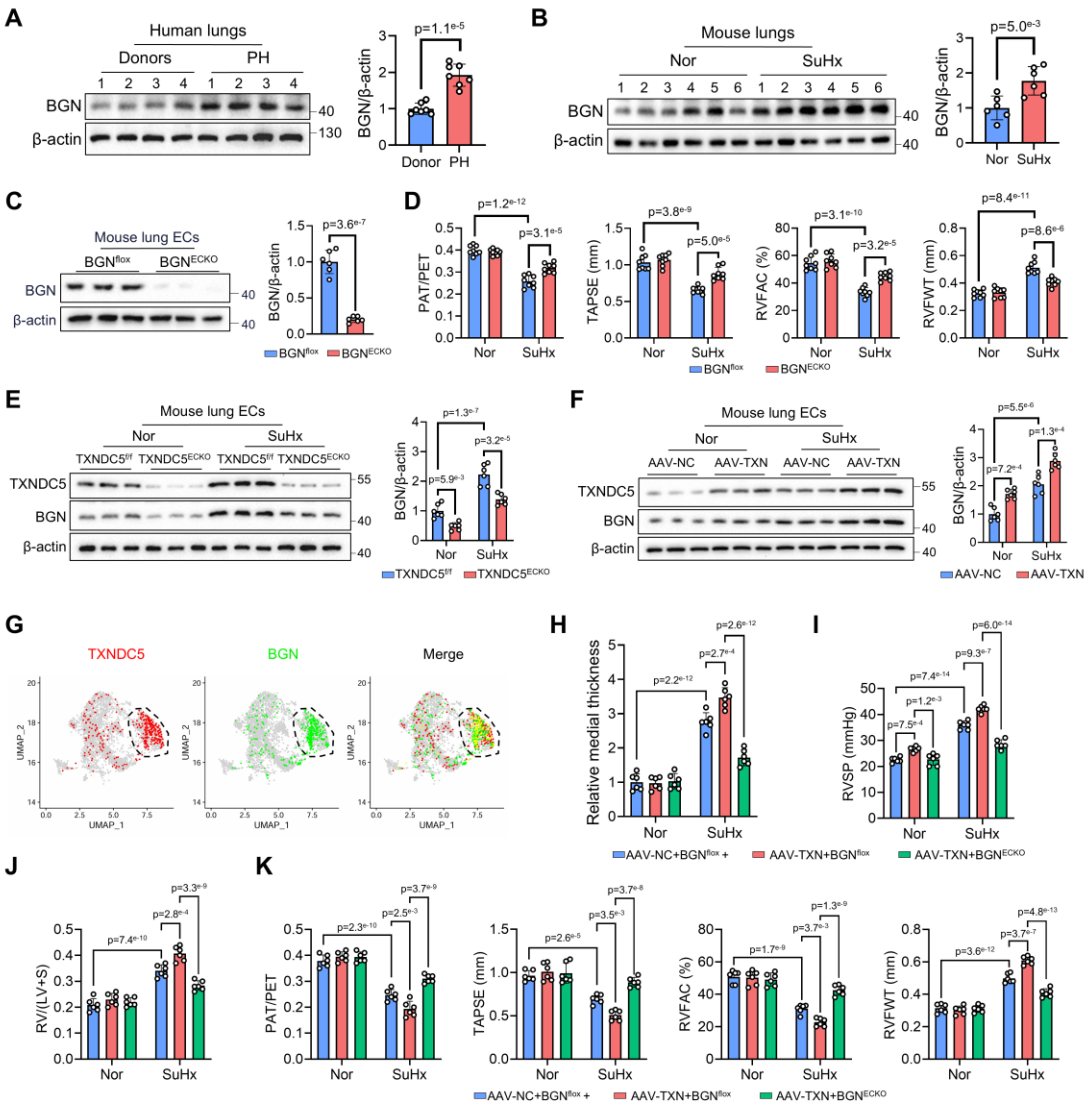

Figure S5. **BGN mediated TXNDC5-driven ECM regulation and PH development.** **A** and **B**, Western blots showing BGN protein levels in lung tissue from patients with PH (n=7) and from SuHx-treated mice (n=6). **C**, Western blot analysis showing BGN protein levels in isolated lung endothelial cells (ECs) from BGN^{ECKO} mice and BGN^{flox}

controls (n=6). **D**, Echocardiographic assessment indicated that SuHx-induced right ventricular dysfunction was attenuated in BGN^{ECKO} mice compared with BGN^{flox} controls (n=6). **E**, Western blot analysis showing BGN protein levels in lung ECs from $TXNDC5^{f/f}$ and $TXNDC5^{ECKO}$ mice under normoxia or SuHx conditions (n=6). **F,** Western blot analysis showing BGN expression in lung ECs following endothelial TXNDC5 overexpression (AAV-TXN) (n=6). **G**, UMAP feature plot showing the distribution of TXNDC5 and BGN expression in $TXNDC5^{high}$ ECM-producing ECs. **H**, Quantification of pulmonary arterial medial wall thickness based on hematoxylin and eosin (H&E) staining in BGN^{flox} and BGN^{ECKO} mice following endothelial TXNDC5 overexpression (n=6). **I**, Measurement of right ventricular systolic pressure (RVSP) in BGN^{flox} and BGN^{ECKO} mice following endothelial TXNDC5 overexpression (n=6). **J**, Fulton index [RV/(LV+S)] in BGN^{flox} and BGN^{ECKO} mice (n=6). **K**, Echocardiographic analysis showing right ventricular function parameters in BGN^{flox} and BGN^{ECKO} mice following endothelial TXNDC5 overexpression (n=6). Data represent the mean±SD. Comparisons of parameters were performed with the unpaired 2-tailed Student *t*-test (**A-C**) or 2-way ANOVA (**D-F** and **H-K**), followed by Tukey honestly significant difference test for multiple comparisons. Nor indicates normoxia; Hyp, hypoxia; SuHx, and Sugen5416/hypoxia.